AGU PUBLICATIONS

JGR

Journal of Geophysical Research: Atmospheres

RESEARCH ARTICLE
10.1002/2014JD022646

Key Points:
- Albedo reduction by dust or black carbon depends on snow grain size
- The presence of dust mutes the influence of black carbon on snow albedo
- Dust can be represented by a scaled black carbon amount

Supporting Information:
- Figures S1–S5
- Table S1

Correspondence to:
C. Dang,
chengd1@atmos.washington.edu

Citation:
Dang, C., R. E. Brandt, and S. G. Warren (2015), Parameterizations for narrowband and broadband albedo of pure snow and snow containing mineral dust and black carbon, *J. Geophys. Res. Atmos.*, *120*, doi:10.1002/2014JD022646.

Received 2 OCT 2014
Accepted 7 APR 2015
Accepted article online 10 APR 2015

Parameterizations for narrowband and broadband albedo of pure snow and snow containing mineral dust and black carbon

Cheng Dang[1], Richard E. Brandt[2], and Stephen G. Warren[1]

[1]Department of Atmospheric Sciences, University of Washington, Seattle, Washington, USA, [2]Atmospheric Sciences Research Center, State University of New York at Albany, Albany, New York, USA

Abstract The reduction of snow spectral albedo by black carbon (BC) and mineral dust, both alone and in combination, is computed using radiative transfer modeling. Broadband albedo is shown for mass fractions covering the full range from pure snow to pure BC and pure dust, and for snow grain radii from 5 μm to 2500 μm, to cover the range of possible grain sizes on planetary surfaces. Parameterizations are developed for opaque homogeneous snowpacks for three broad bands used in general circulation models and several narrower bands. They are functions of snow grain radius and the mass fraction of BC and/or dust and are valid up to BC content of 10 ppm, needed for highly polluted snow. A change of solar zenith angle can be mimicked by changing grain radius. A given mass fraction of BC causes greater albedo reduction in coarse-grained snow; BC and grain radius can be combined into a single variable to compute the reduction of albedo relative to pure snow. The albedo reduction by BC is less if the snow contains dust, a common situation on mountain glaciers and in agricultural and grazing lands. Measured absorption spectra of mineral dust are critically reviewed as a basis for specifying dust properties for modeling. The effect of dust on snow albedo at visible wavelengths can be represented by an "equivalent BC" amount, scaled down by a factor of about 200. Dust has little effect on the near-IR albedo because the near-IR albedo of pure dust is similar to that of pure snow.

1. Introduction

The albedo α of snow varies greatly with wavelength λ [*Wiscombe and Warren*, 1980; *Grenfell et al.*, 1994], because the absorption coefficient of ice varies by 7 orders of magnitude across the solar spectrum [*Warren and Brandt*, 2008]. The most important snowpack variable influencing the albedo is the ratio of the surface area of snow grains to the mass of snow, the "specific surface area" [e.g., *Matzl and Schneebeli,* 2006, 2010]. The specific surface area (β) can be converted to a radiatively effective snow grain radius r, the same as the "effective radius" that *Hansen and Travis* [1974] defined for a size distribution of spheres:

$$\beta = 3/(r\rho_{\mathrm{ice}}), \tag{1}$$

where ρ_{ice} is the density of pure ice, 917 kg m^{-3}. The snow grain size normally increases as the snow ages [*LaChapelle*, 1969]. Coarse-grained snow (smaller specific surface area) has lower albedo than fine-grained snow, and the differences in albedo are greatest in the near-infrared region around $\lambda \approx 1$ μm, where $\alpha \approx 0.5$ [*Wiscombe and Warren*, 1980].

Integrated over the solar spectrum, the broadband albedo of pure deep snow is in the range 0.7–0.9, higher than that of any other natural surface. This is because at visible wavelengths, where the solar energy spectrum peaks, ice is almost nonabsorptive, so incident photons survive refraction through many snow grains to reemerge at the surface. Because ice absorption is so weak at visible wavelengths, in this spectral region the absorption of sunlight in natural snow is mostly due to absorptive impurities that are incorporated during ice nucleation in clouds, scavenging by falling snow crystals below the cloud, and dry deposition of aerosol to the snowpack surface. In many geographical regions the most important light-absorbing impurity (LAI) in snow is black carbon (BC); in others brown carbon (organic carbon) or mineral dust may dominate [*Painter et al.,* 2007; *Doherty et al.,* 2010, 2014; *Zhang et al.*, 2013; *Wang et al.,* 2013]. For example, BC contributes ~60% of the particulate light absorption in Arctic snow [*Doherty et al.,* 2010] and ~70% in northeast China [*Wang et al.,* 2013], but dust dominates in Inner Mongolia. However, as indicated above, snow albedo is usually influenced more by grain growth than by impurities. The increase

of grain radius from $r = 100$ μm in new snow to $r = 1000$ μm in old melting snow causes a decrease in all-wave albedo by 12%, whereas a typical BC mixing ratio observed in remote snow in the Arctic and midlatitudes, 20 ng/g, lowers all-wave albedo by 0.5% for $r = 100$ μm or 1.6% for $r = 1000$ μm.

The importance of BC for snow albedo was noted by *Warren and Wiscombe* [1980, 1985], and a first survey of BC in Arctic snow was carried out by *Clarke and Noone* [1985]. Recently, there has been a renaissance of research into radiative forcing by LAI in snow, following the assessment by *Hansen and Nazarenko* [2004] that radiative forcing by anthropogenic BC via reduction of snow albedo has the highest "efficacy" of any forcing agent, and speculation that it could be responsible for a significant part of Arctic climate change. Related work now includes modeling, field work, and laboratory studies [e.g., *Jacobson*, 2004; *Flanner et al.,* 2007, 2009; *Koch et al.,* 2009; *Doherty et al.,* 2010, 2013, 2014; *Ye et al.,* 2012; *Forsström et al.,* 2009; *Hagler et al.,* 2007; *McConnell et al.,* 2007; *Ming et al.,* 2009; *Brandt et al.,* 2011; *Hadley and Kirchstetter*, 2012; *Hegg et al.,* 2010; *Warren*, 2013]. The results of many of these studies were reviewed by *Bond et al.* [2013].

Several climate modeling efforts are underway to assess the climatic effects of LAI in Northern Hemisphere snow. For snow albedo, those models incorporate parameterizations of varying complexity and accuracy, depending on the application, for each of the spectral bands of a general circulation model (GCM). Many GCMs break the solar spectrum into just two bands, 0.2–0.7 μm and 0.7–4.0 μm, and therefore require simple functions to compute band-average albedo. Snow albedo depends on grain size, depth (as snow water equivalent), cloud cover and cloud optical thickness, solar zenith angle, and impurities. If the snowpack is thin, the surface albedo is also affected by the albedo of the underlying surface and by vegetation protruding through the snowpack. In this work we avoid that complexity by developing parameterizations only for snowpacks that are thick enough to hide the underlying surface at all wavelengths (optically "semi-infinite"). Furthermore, we compute broadband albedos for only two atmospheric conditions with their accompanying solar spectra: under clear sky with solar zenith angle $\theta_o = 49.5°$ (with cosine $\mu_o = 0.65$) and under overcast cloud with visible optical depth $\tau = 11$. The angle 49.5° is the effective zenith angle for diffuse radiation under cloud [*Marshall and Warren*, 1987]. The value $\mu_o = 0.65$ is also very close to the insolation-weighted average μ for the sunlit hemisphere of Earth, which is a cosine-weighed mean cosine, $\mu = 2/3$, corresponding to $\theta = 48.2°$. This choice will turn out to be useful below where we parameterize the zenith angle dependence of snow albedo.

The solar spectral irradiances we use are for Arctic summer. The only impurities we consider are BC and mineral dust, each with only one size distribution, but the albedo reduction by organic carbon may be mimicked by mineral dust, because they have similar absorption spectra (stronger absorption at UV and blue wavelengths and weaker absorption at red wavelengths) [*Doherty et al.,* 2010].

Our aim is to produce the simplest possible parameterizations that can represent the most important controlling variables, snow grain size and impurities, with a requirement that they cover the full range of impurity concentrations to be found in snow. We have made simplicity a design criterion for our parameterizations because we envision their incorporation into GCMs that are used for long time integrations, for which computation time must be minimized and which in any case allocate only a small fraction of computer time to consideration of snow. Other more complex parameterizations are available, which may be preferable for some purposes. The parameterization of *Marshall and Warren* [1987] and *Marshall* [1989] parameterizes albedo in two bands as functions of snow grain size, solar zenith angle, cloud transmittance, snow depth, underlying surface albedo, and BC content. It was used in a GCM by *Marshall and Oglesby* [1994]. *Gardner and Sharp* [2010] developed a parameterization for the total broadband solar albedo but not for separate visible and near-infrared bands. They reviewed some other parameterizations and showed good agreement of their own work with the parameterization of *Marshall and Warren* [1987]. The zenith angle parameterization developed by *Marshall and Warren* [1987] is incorporated below in our work. Teruo Aoki and his coworkers [*Aoki et al.,* 2011; *Niwano et al.,* 2012; *Yasunari et al.,* 2011, 2014], recognizing the primary influence of snow grain size on albedo, have developed parameterizations of grain growth as a function of snow age and temperature history.

Some GCMs may actually have no need for a snow albedo parameterization. The SNICAR model of *Flanner et al.* [2007] computes the entire albedo spectrum at fine wavelength resolution and then integrates it over whatever band is desired. The SNICAR model has been incorporated as a subroutine in the standard implementation of National Center for Atmospheric Research's (NCAR's) Community Earth System Model

[*Lawrence et al.,* 2011, 2012*; Holland et al.,* 2012]. SNICAR can also be run conveniently from a website, http://snow.engin.umich.edu/.

The parameterization presented here is distinguished from previous work by the following. (1) We plot albedo for the full range of impurity content, from pure snow to pure dust and pure BC, and develop parameterizations valid up to 10 ppm of BC. (2) We show how to combine dust and BC as a "BC-equivalent" mass mixing ratio, for their combined effect on albedo reduction. (3) We develop parameterizations for multiple spectral bands in GCMs that use more than two bands. (4) We carry out a review of optical properties of different mineral dusts, with guidance on how to change our parameterization if a different type of dust is desired to replace our choice. (5) We provide a single metric that quantitatively displays how grain size interacts with impurity content to determine the albedo reduction.

The essence of our work is an update and expansion of Figures 1 and 2 of *Warren and Wiscombe* [1985], which have found use in climate modeling [e.g., *Koch et al.,* 2009].

We consider only particulate impurities; the effects of soluble impurities are probably insignificant by comparison in most locations, as summarized by *Dang and Hegg* [2014]: Soluble impurities in snow ("chromophores") were studied by *Beine et al.* [2011] at Barrow, Alaska; their results show that the soluble impurities absorb significantly at ultraviolet wavelengths (200–300 nm) but much less at the longer wavelengths where solar energy peaks. Figure 1 of *Beine et al.* [2011] shows the absorption coefficient (on base 10) versus wavelength for a typical sample of meltwater. The absorption by soluble impurities at 400 nm is equivalent to that of 0.14 ng/g BC; at the midvisible wavelength 550 nm the absorption is equivalent to 0.07 ng/g BC. The BC mixing ratio at Barrow before onset of melt is 10–30 ng/g [*Doherty et al.,* 2013], similar to the values found elsewhere in North America [*Doherty et al.,* 2014], and particulate non-BC is responsible for comparable absorption. We conclude that absorption by the soluble organics is negligible in comparison.

Our strategy for development of parameterizations is to run an accurate radiative transfer model (discrete ordinates radiative transfer, DISORT) for numerous combinations of the relevant variables and then to fit the model results to simple analytical functions. We make use of measurements only indirectly, in that we have carried out one controlled experiment on an artificial snowpack with added soot, and its spectral albedo was consistent with the DISORT calculation [*Brandt et al.,* 2011]. But for such measurements to be used directly in parameterization development, numerous snowpacks with varying combinations of different grain sizes and different BC amounts would have to be produced and measured spectrally. Such a massive experimental effort is not forthcoming, so we instead develop our parameterization using radiative transfer modeling.

2. Solar Spectra Used for the Spectral Integrations

The broadband albedo α is an irradiance-weighted average of the spectral albedo α_λ:

$$\alpha = \frac{\int \alpha_\lambda S(\lambda) d\lambda}{\int S(\lambda) d\lambda}, \tag{2}$$

where $S(\lambda)$ is the incident solar spectrum and the limits of integration are those of the band under consideration. We use two solar spectra characteristic of high-latitude climate during the sunlit seasons, one clear and one cloudy. They were measured at the surface of the Arctic Ocean during summer by *Grenfell and Perovich* [2008]. The measurements covered the wavelength range 0.35–2.5 μm; they are extended to 4.0 μm by the use of the atmospheric model SBDART [*Ricchiazzi et al.,* 1998] for the subarctic summer standard atmosphere [*McClatchey et al.,* 1972]. The Grenfell-Perovich cloudy case can be matched by specifying a cloud of visible optical depth $\tau = 11$ in SBDART, which is typical for Arctic summer stratus clouds [*Tsay and Jayaweera,* 1984]. The principal results of this paper, namely, the reduction of snow albedo caused by BC and dust, turn out to be quite insensitive to the difference between the measured and modeled incident solar spectra. The spectra we use are shown in Figure 1.

3. Albedo of Pure Snow

We use spectral optical constants of ice from the revised compilation of *Warren and Brandt* [2008]. We use Mie theory [*Wiscombe*, 1980] to compute extinction efficiency Q_{ext}, single-scattering albedo ϖ, and asymmetry parameter g for ice spheres of radii 5–2500 μm. For fluxes and albedo (not directional

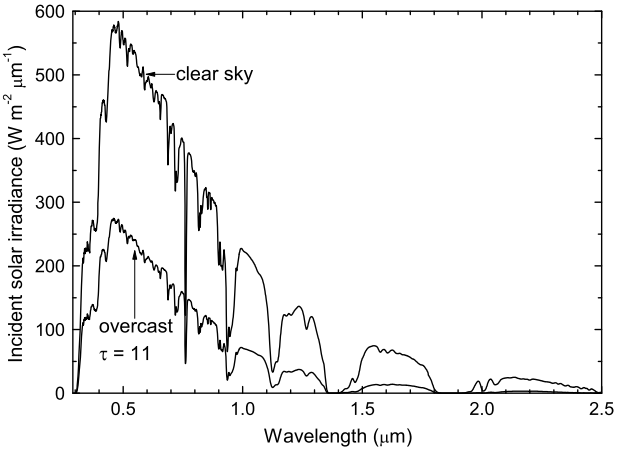

Figure 1. Incident solar spectra used for spectral integrations to get broadband albedos (equation (2)). These spectra were measured at the sea surface in the Arctic Ocean during summer under clear sky and under overcast cloud by *Grenfell and Perovich* [2008].

quantities), a nonspherical ice crystal can be represented by a collection of spheres with the same volume-to-area ratio; the accuracy of this representation was evaluated by *Grenfell and Warren* [1999], *Neshyba et al.* [2003], and *Grenfell et al.* [2005], who showed good accuracy for Q_{ext} and ϖ but discrepancies for g. A size distribution of snow grains is represented by the area-weighted mean radius, called the effective radius. Scattering and absorption calculated using effective radii have been shown to accurately reproduce scattering and absorption calculated with full particle size distributions [*Hansen and Travis,* 1974]. The range of sizes considered here spans the effective radii of surface snow on Earth, which are rarely smaller than 30 μm or larger than 1000 μm [*LaChapelle*, 1969], and allows for application to other planetary surfaces that may have smaller or larger grains. The plots of single-scattering quantities Q_{ext}, $1-\varpi$, and g are similar to those published by *Wiscombe and Warren* [1980]; they are shown in the supporting information.

The spectral albedo of pure deep snow is then computed using the discrete ordinates method (DISORT [*Stamnes et al.,* 1988]) and is shown in several of the figures below as the reference plot from which reductions due to LAI are determined. The results for pure snow deviate slightly from those of *Wiscombe and Warren* [1980], but the deviations are mainly due to the use of the new compilation of ice absorption coefficient [*Warren and Brandt*, 2008]; the use of DISORT rather than the delta-Eddington method for the radiative transfer had little effect.

Band albedos are shown in Figure 2. They are parameterized as quadratic functions of snow grain radius:

$$\alpha(r) = m_0 + m_1 r_n + m_2 r_n^2, \tag{3}$$

$$\text{where} \quad r_n \equiv \log_{10}(r/r_0), \tag{4}$$

representing the relative deviation from a reference baseline grain radius $r_o = 100$ μm. The coefficients are given in Table 1.

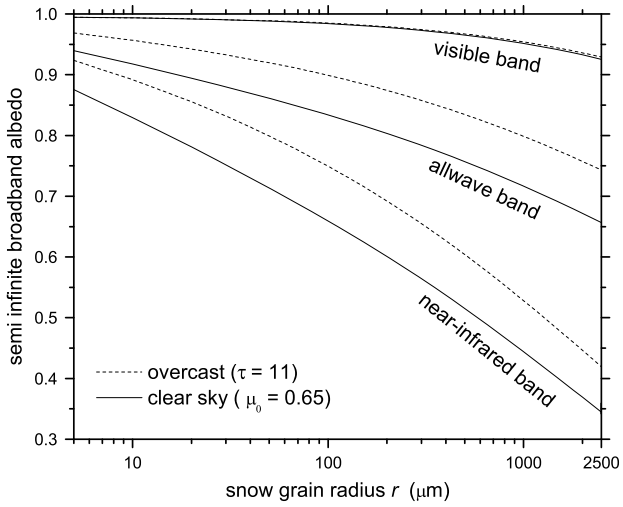

Figure 2. Broadband albedo of pure deep snow as a function of optically effective snow grain radius, for three bands: visible (0.3–0.7 μm), NIR (0.7–4.0 μm), and all-wave (0.3–4.0 μm), each for both clear sky and overcast sky.

The albedos are slightly higher than in our earlier work, because the absorption coefficient of ice in the wavelength region 300–600 nm is smaller in the revised compilation [*Warren and Brandt*, 2008] than in the compilation used earlier [*Warren*, 1984].

3.1. Effect of Zenith Angle

Marshall and Warren [1987] and *Marshall* [1989] showed that the spectral signature of albedo reduction caused by moving the Sun to a higher elevation resembles that caused by increasing the snow grain size. This is because in both cases the reason for the albedo reduction is that solar photons penetrate deeper into the snow before their first scattering event. The two

Table 1. Parameterization for Broadband Albedo α of Pure Snow as a Function of Snow Grain Radius r, Relative to $r_o = 100$ μm[a]

Band	m_0	m_1	m_2
	Clear Sky		
All-wave 0.3–4.0 μm	0.8344	−0.1007	−0.0177
Visible 0.3–0.7 μm	0.9849	−0.0215	−0.0132
Near-IR 0.7–4.0 μm	0.6596	−0.1927	−0.0229
	Overcast Cloud		
All wave 0.3–4.0 μm	0.8994	−0.0793	−0.0221
Visible 0.3–0.7 μm	0.9856	−0.0202	−0.0125
Near-IR 0.7–4.0 μm	0.7493	−0.1820	−0.0388

[a]The albedo α is given as $\alpha = m_0 + m_1 r_n + m_2 r_n^2$, where $r_n \equiv \log_{10}(r/r_o)$. The coefficients are given above. Coefficients are also available for RRTM bands in the supporting information.

variables can therefore be combined into a single predictor for snow albedo. *Marshall* [1989] did this by defining a standard zenith cosine, $\mu_D = 0.65$ (zenith angle $\theta = 49.5°$), which is the effective zenith angle for diffuse radiation (meaning that snow albedo for diffuse incidence is the same as the albedo for a direct beam at $\mu = 0.65$). For a direct beam at angle μ incident on a snowpack with grain radius r, the snow albedo is close to that for Sun at μ_D and an altered grain radius r' [*Marshall,* 1989, equation (2.4)]:

$$r' = r(1 + a\ \Delta\mu)^2, \tag{5}$$

where $\Delta\mu \equiv \mu - \mu_D$; values of a are 0.781 (visible), 0.791 (near-IR), and 0.786 (all wave).

The reference value $\mu_D = 0.65$ is also close to the insolation-weighted solar zenith cosine for the sunlit hemisphere of a planet, $\mu = 2/3$. All our plots for clear-sky albedo are for $\mu = \mu_D = 0.65$; values for other zenith angles under clear sky can be obtained by altering the snow grain radius using equation (5).

4. Single-Scattering by Black Carbon Particles

The spectral scattering and absorption properties of BC particles (intrinsic optical properties, IOPs) depend on the density of the BC composing a particle, the spectral complex refractive index, and the size distribution [*Bond and Bergstrom*, 2006]. When BC particles are embedded in a snowpack, their IOPs additionally depend on their microlocation, whether inside snow grains ("internally mixed"), or in interstitial spaces between snow grains ("externally mixed"), or on the surfaces of snow grains [*Ackerman and Toon*, 1981; *Fuller et al.,* 1999; *Flanner et al.,* 2012]. Our modeling uses Mie theory assuming external mixtures; an internal mixture has greater absorption, by a factor of 1.8–2.1 [*Flanner et al.,* 2012]; this scale factor can be applied to our results if an internal mixture is to be modeled. Figure 3 shows computed IOPs for four different size distributions of BC, described by their mass-mean diameters (D_{mm}) and effective radii (r_{eff}). All size distributions in these calculations are lognormal, with geometric width $\gamma_g = 1.3$ [*Clarke et al.,* 1987].

For our computations with BC we use complex refractive index $m = 1.95–0.79i$, independent of wavelength, and density $\rho = 1.8\ \mathrm{g\ cm^{-3}}$, as recommended by *Bond and Bergstrom* [2006]. They reviewed measurements of $m(\lambda)$ and concluded that within experimental error, there was no evidence for a wavelength dependence of m [*Bond and Bergstrom,* 2006, section 7.6]. The extinction efficiency Q_{ext} (Figure 3a) decreases with wavelength; for $\lambda \gg D_{\mathrm{mm}}$ the particles are in the Rayleigh limit and Q_{ext} is proportional to λ^{-4}. The single-scattering albedo ϖ (Figure 3b) also decreases with λ as the BC particles become pure absorbers in the Rayleigh limit. The asymmetry parameter g (Figure 3c) also decreases with wavelength, as the Rayleigh scattering phase function is forward-backward symmetric. The quantities Q_{ext} and ϖ, in combination with r_{eff} and the particle density ρ, determine the mass absorption cross-section (sometimes called "mass absorption efficiency") B_a, with units $\mathrm{m^2/g}$, shown in Figures 3d and 3e:

$$B_a = \frac{Q_{\mathrm{ext}} \pi r_{\mathrm{eff}}^2 (1 - \varpi)}{\frac{4}{3}\pi r_{\mathrm{eff}}^3 \rho} = \frac{3 Q_{\mathrm{ext}} (1 - \varpi)}{4 r_{\mathrm{eff}} \rho}. \tag{6}$$

A size distribution with $D_{\mathrm{mm}} = 0.13$ μm was chosen to represent ambient atmospheric soot [*Clarke et al.,* 1987]; all subsequent results in this paper use this distribution. Together with our choices for ρ and m, this size distribution has $B_a = 6.73\ \mathrm{m^2/g}$ at $\lambda = 550$ nm, which is toward the low end of the range recommended by *Bond and Bergstrom* [2006] for atmospheric BC, $B_a = 7.5 \pm 1.2\ \mathrm{m^2/g}$. As Figure 3d shows, B_a at 550 nm (as a function of D_{mm}) peaks at $D_{\mathrm{mm}} \approx 130$ nm, so higher values of B_a can be obtained only by altering ρ or m away from the ranges recommended by Bond and Bergstrom. *Flanner et al.* [2009] did adjust the BC

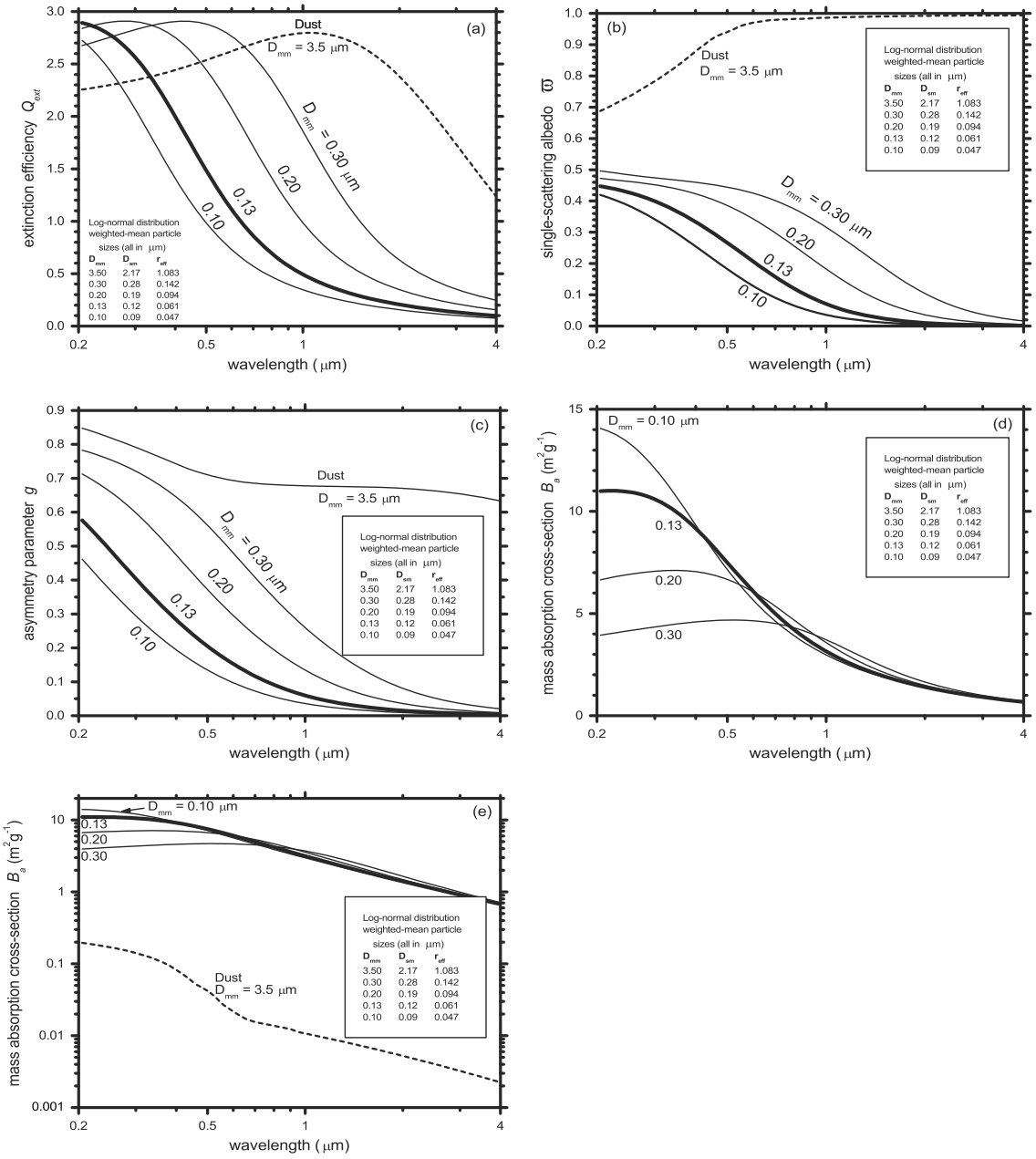

Figure 3. Single-scattering quantities for BC and mineral dust: (a) extinction efficiency Q_{ext}, (b) single-scattering albedo ϖ, (c) asymmetry parameter g, (d) mass absorption cross-section B_a, and (e) mass absorption cross-section B_a on a logarithmic scale so as to display both dust and BC together. Results are plotted for four different size distributions of BC, labeled by their mass-mean diameters (D_{mm}). The corresponding surface-mean diameters D_{sm} and effective radii (r_{eff}) are given in the legend. The plots for $D_{mm} = 0.13$ μm are shown in bold; they are used in the multiple-scattering calculations for mixtures of BC and snow.

density to obtain $B_a = 7.5\ m^2/g$ at $\lambda = 550$ nm, but we have not done so. We think that the lower value we obtain for B_a is probably more appropriate for BC in snow because BC particles aggregate in snow to larger sizes [*Schwartz et al.,* 2013], which would have smaller B_a (Figure 3d).

Figure 3e shows that B_a for BC decreases with wavelength, paralleling the decrease of Q_{ext} in the Rayleigh regime. The B_a for dust parallels that for BC, but dust particles are larger and not in the Rayleigh limit, so the spectral behavior for dust has a different explanation, namely, that the absorption coefficient of pure dust decreases with wavelength, as will be shown below in section 6.

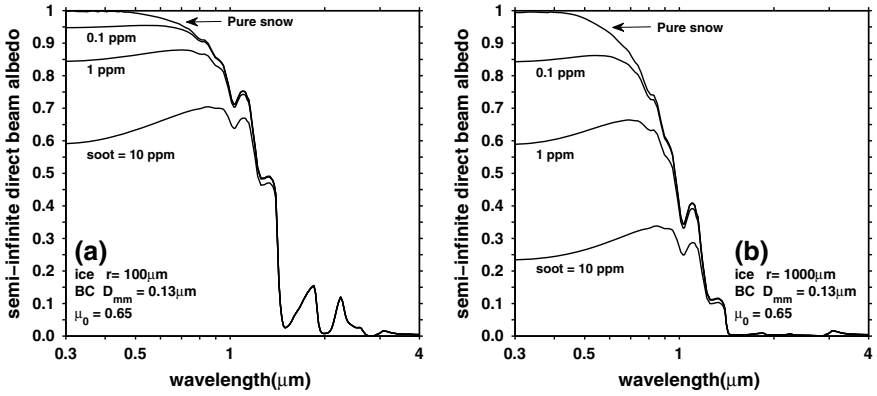

Figure 4. Spectral albedo (for a direct solar beam) of pure snow and of snow containing BC in three mixing ratios. Snow grain radii (a) $r = 100$ μm and (b) $r = 1000$ μm.

5. Albedo of Snow Containing Black Carbon

The single-scattering quantities, computed separately for ice particles and black carbon particles (both represented by spheres), must be combined according to their specified mass fractions. In this work, we assume that the snowpack consists of ice particles and BC particles in an "external mixture"; i.e., both are surrounded by air. Therefore, the single-scattering quantities of the snowpack are just averages of the single-scattering quantities of snow and BC, weighted by their cross-sectional areas and scaled by their mass fractions. The procedure for doing this is given in the appendix. How the results would change for an internal mixture was discussed above in section 4.

5.1. Spectral Albedo

Figure 4 shows the albedo for pure snow and for snow with added BC in three mixing ratios. For $\lambda < 1$ μm, BC causes a reduction of albedo; at longer wavelengths ice itself is strongly absorptive, so small amounts of absorptive impurities have little effect. For a given BC mixing ratio, the reduction of albedo is greater in coarse-grained snow (Figure 4b) than in fine-grained snow (Figure 4a), as was first shown by *Warren and Wiscombe* [1980]. For small BC mixing ratios, albedo is nearly flat across the visible and near ultraviolet (near UV). For very large BC mixing ratios the albedo shows a reddening because of the greater absorption by BC at shorter wavelengths (Figure 3d). Figure 4 resembles Figure 7 of *Warren and Wiscombe* [1980]; the differences are due to the use of new optical constants for ice and different physical and optical properties of BC.

5.2. Broadband Albedo

The reduction of broadband snow albedo caused by BC is plotted in Figure 5 for three wavelength bands, using the clear-sky solar spectrum. These values, as well as those for snow under cloud, are fitted to cubic or quadratic functions of the BC mixing ratio C relative to a reference value $C_o = 10^{-6}$; the coefficients in turn are quadratic functions of snow grain radius.

In choosing a parameterization for albedo reduction $\Delta\alpha$, we are guided by measurements showing the range of BC mixing ratios to be expected, usually expressed as ng/g, equivalent to ppb by mass. Typical BC mixing ratios are 0.1–0.7 ng/g on Antarctica [*Warren and Clarke*, 1990], 2–4 ng/g on the Greenland Ice Sheet, 10–30 ng/g in low-elevation Arctic regions [*Doherty et al.,* 2010], and 20–100 ng/g in midlatitude North America [*Doherty et al.,* 2014]. However, mixing ratios as high as 2000 ng/g are found in northeast China [*Huang et al.,* 2011; *Wang et al.,* 2013], so we offer parameterizations valid up to 10,000 ng/g (10 ppm). To maintain accuracy without the need for higher-order terms, we have developed separate parameterizations for high and low BC mixing ratios ("Range 1," 100 ppb–10 ppm and "Range 2," <300 ppb). The two parameterizations overlap in the range 100–300 ppb, where both are accurate.

The coefficients for the parameterizations are given in Table 2. The parameterizations are functions of log C, so they cannot be used directly as C approaches zero. Therefore, for each spectral interval we determine, as a function of snow grain size, the minimum value of C for which the Range 2 parameterization is applicable; then we linearly interpolate $\Delta\alpha$ down to $\Delta\alpha = 0$ at $C = 0$ ("Range 3" in Table 2).

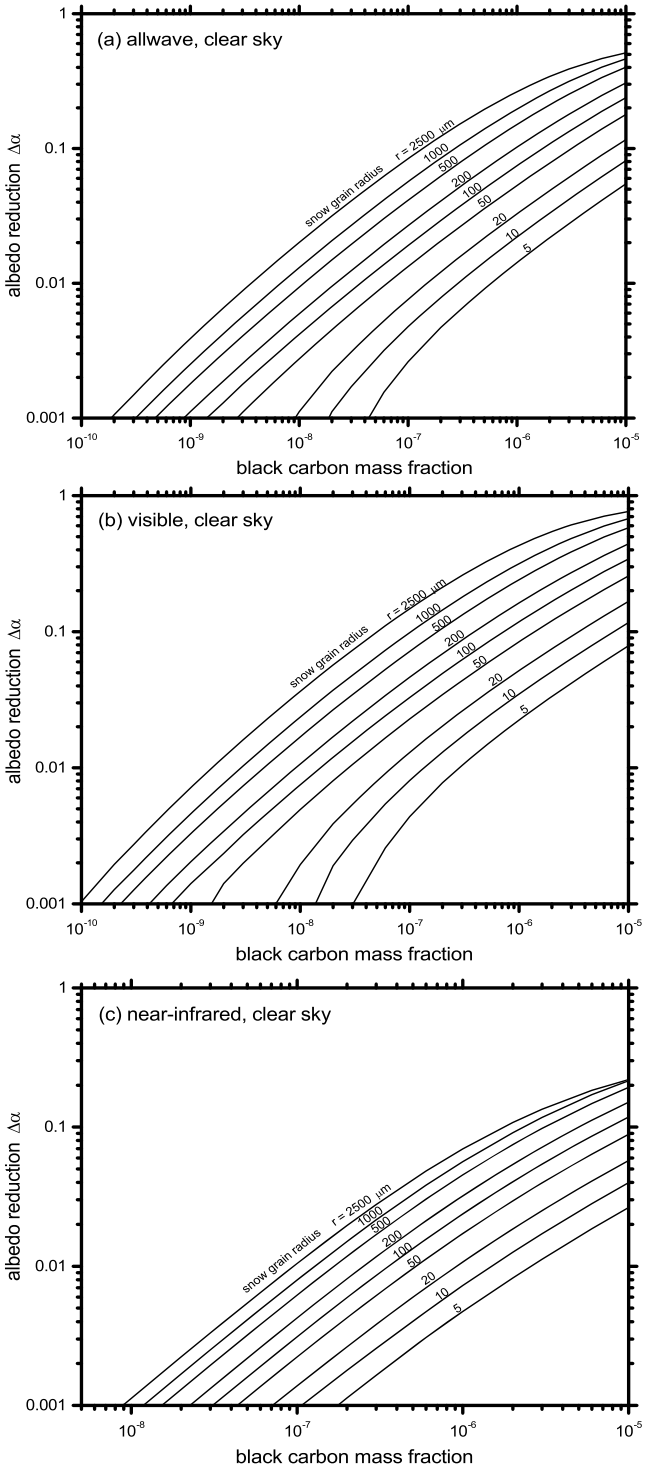

Figure 5. Reduction in clear-sky broadband albedo ($\Delta\alpha$) caused by the addition of BC to snow, as a function of the mass fraction of BC, for eight different snow grain radii from 5 μm to 2500 μm. (a) All-wave, (b) visible band, and (c) near-infrared band.

The errors caused by the use of the parameterization are plotted in the supporting information. The maximum absolute error is <0.001 for most combinations of r and C; it slightly exceeds 0.005 for the combination of large r and large C ($r > 1000\,\mu$m and $C > 1000$ ng/g).

5.3. Combination of Snow Grain Size and BC Content Into a Single Predictor

A given BC mixing ratio causes a greater albedo reduction in coarse-grained snow than in fine-grained snow. The albedo reduction $\Delta\alpha$ caused by a given BC mixing ratio C in snow of grain size r could alternatively be caused by a smaller C if the snow grain size is larger. In fact, the curves in Figure 5 parallel each other, suggesting that snow grain size and BC mixing ratio might be combined into a single predictor for the BC-induced albedo reduction, for quick hand calculations. (Note that here we are predicting not the albedo but rather the BC-induced albedo reduction.) Indeed, this can be done, with only slight loss of accuracy. To do so, we define a single parameter H, which accounts for changes in both BC mixing ratio and snow grain size:

$$H \equiv \left(\frac{C}{C_0}\right)\left(\frac{r}{r_0}\right)^s. \tag{7}$$

We vary s until the curves in Figure 5 merge to a single curve, obtaining $s = 0.73$ for all-wave and visible and $s = 0.43$ for near-IR (Figure 6). This means that for all-wave albedo or visible albedo, a twofold increase of C causes the same change in BC-induced albedo reduction as multiplying r by 2.6. For the near-IR a twofold increase in C can be mimicked by a fivefold increase in r.

Plots of albedo reduction versus H (Figure 6) for the all-wave, visible, and near-IR bands are fitted to quadratic functions of $p \equiv \log_{10} H$:

$$\Delta\alpha_n \equiv \log_{10}(\Delta\alpha) = m_1 p^2 + m_2 p + m_3, \tag{8}$$

whose coefficients are given in Table 3. This parameterization is valid for $50 < r < 2500\,\mu$m and for ranges of H that are different for the different wavelength bands, as given in Table 3. The use of the simplified parameterization in

Table 2. Parameterization for Broadband Albedo Reduction Due To BC

(a) *Definitions of Parameters*

Parameter	Definition
r	snow grain radius (μm)
r_o	100 μm
C	black carbon mass fraction
C_0	10^{-6}
r_n	$\log_{10}(r/r_0)$
C_n	$\log_{10}(C/C_0)$
$\Delta\alpha$	reduction from the albedo of pure snow
$\Delta\alpha_n$	$\log_{10}[\Delta\alpha]$

(b) *Domains of Broadband Albedo Parameterizations, Defined by Illumination Wavelength Band and Mass Fraction C of Black Carbon*

Band Boundaries (μm)	Range 1 ($10^{-7} < C < 10^{-5}$)	Range 2 ($C_{low} \le C < 3\times10^{-7}$)	Range 3 ($0 < C \le C_{low}$)
All-wave (0.3–4.0)	Cubic functions: $\Delta\alpha_n = f(C_n)$		Linear function $\Delta\alpha = f(C)$
Visible (0.3–0.7)	Coefficients are quadratic functions of r_n		
Near-IR (0.7–4.0)	Quadratic functions: $\Delta\alpha_n = f(C_n)$ Coefficients are quadratic functions of r_n		

(c) *Functional Forms of Parameterizations*

For Ranges 1 and 2 the parameterization is

$$\log_{10}\Delta\alpha = q_0 + q_1 C_n + q_2 {C_n}^2$$

where the q_i are quadratic/cubic functions of r:

$$q_2 = p_{4,1} + p_{3,1} r_n + p_{2,1} {r_n}^2 + p_{1,1} {r_n}^3$$
$$q_1 = p_{4,2} + p_{3,2} r_n + p_{2,2} {r_n}^2 + p_{1,2} {r_n}^3$$
$$q_0 = p_{4,3} + p_{3,3} r_n + p_{2,3} {r_n}^2 + p_{1,3} {r_n}^3$$

For the near-IR a quadratic function is sufficient, so $p_{1,i} = 0$.
A minimum value of C, called C_{low}, is determined for Range 2, below which a linear function is used (Range 3); C_{low} is a quadratic function of r_n:

$$C_{low} = j_1 + j_2 r_n + j_3 {r_n}^2.$$

The coefficients j are given below. For BC mixing ratio lower than C_{low}, $\Delta\alpha$ is calculated by linear interpolation between $C = C_{low}$ and $C = 0$:

$$\Delta\alpha = t \ \ C/C_{low},$$

where the t is the albedo reduction produced by C_{low}; the values of t are listed below.

(d) *Coefficients for the Parameterizations*

Range 1 ($10^{-7} < C < 10^{-5}$)

	Clear sky (sza = 49.5°)				Overcast sky		
	$p_{row,1}$	$p_{row,2}$	$p_{row,3}$		$p_{row,1}$	$p_{row,2}$	$p_{row,3}$
All-wave 0.3–4 μm	0.0068	−0.0188	−0.0003	All-wave 0.3–4 μm	0.0080	−0.0190	−0.0002
	−0.0257	−0.0114	−0.0575		−0.0263	−0.0099	−0.0584
	−0.0217	−0.0586	0.4755		−0.0223	−0.0615	0.4747
	−0.0429	0.5501	−1.1265		−0.0437	0.5373	−1.0598
Visible 0.3–0.7 μm	0.0078	−0.0191	0.0006	Visible 0.3–0.7 μm	0.0089	−0.0193	0.0006
	−0.0265	−0.0083	−0.0551		−0.0269	−0.0074	−0.0566
	−0.0229	−0.0595	0.4795		−0.0234	−0.0625	0.4778
	−0.0471	0.5099	−0.9260		−0.0468	0.5045	−0.9192
Near-IR 0.7–4 μm	0	0	0	Near-IR 0.7–4 μm	0	0	0
	−0.0148	−0.0246	−0.0758		−0.0143	−0.0243	−0.0758
	−0.0279	−0.0503	0.4454		−0.0280	−0.0510	0.4452
	−0.0925	0.7936	−1.6215		−0.0960	0.7856	−1.5340

Range 2 ($C_{low} < C < 3\times10^{-7}$)

	$p_{1,row}$	$p_{2,row}$	$p_{3,row}$		$p_{1,row}$	$p_{2,row}$	$p_{3,row}$
All-wave 0.3–4 μm	0.0278	−0.0003	0.0013	All-wave 0.3–4 μm	0.0254	−0.0096	−0.0032
	−0.0762	−0.0761	−0.0756		−0.0801	−0.0767	−0.0760
	0.0465	0.0495	0.5140		0.0575	0.0689	0.5225

Table 2. (continued)

	−0.0420	0.5370	−1.1367		−0.0478	0.5119	−1.0763	
Visible 0.3–0.7 μm	0.0184	−0.0280	−0.0120	Visible 0.3–0.7 μm	0.0243	−0.0180	−0.0073	
	−0.0793	−0.0722	−0.0711		−0.0839	−0.0758	−0.0734	
	0.0729	0.1096	0.5468		0.0680	0.0936	0.5379	
	−0.0592	0.4719	−0.9470		−0.0575	0.4681	−0.9398	
Near-IR 0.7–4 μm 0.0848	0	0	0	Near-IR 0.7–4 μm	0	0	0	
	−0.0077	−0.0139	−0.0720		−0.0090	−0.0169	−0.0733	
	0.0042	−0.0007	0.4631		0.0062	0.0038	0.4656	
	−0.0206	0.9056	−1.5820		−0.0208	0.9038	−1.4919	
				Range 3 ($0 < C < C_{low}$)				
	j_1	j_2	j_3	t		j_1	j_2	j_3	t
All-wave	0.1772	0.8819	−2.8083	0.001	All-wave	0.1997	−0.9173	−2.9212	0.001
Visible	0.2261	−0.9496	−3.1095	0.001	Visible	0.2357	−0.9643	−3.1416	0.001
Near-IR	0.0827	−0.4755	−2.5269	0.0001	Near-IR	0.0848	−0.4773	−2.6194	0.0001

equation (8) instead of the full parameterization of Table 2 causes only small errors. For $C \leq 10^{-6}$ g/g, the all-wave and near-IR albedo errors are <0.01; the visible errors are <0.015.

5.4. Parameterizations for Narrow Bands (Rapid Radiative Transfer Model)

Some GCMs subdivide the solar spectrum into several narrower bands. A popular choice is the set of 14 bands used in the rapid radiative transfer model (RRTM) [*Mlawer and Clough*, 1997]. These bands are listed in Table 4. We do not consider Band 1 (UV) because no solar energy reaches the surface in this band. We also do not

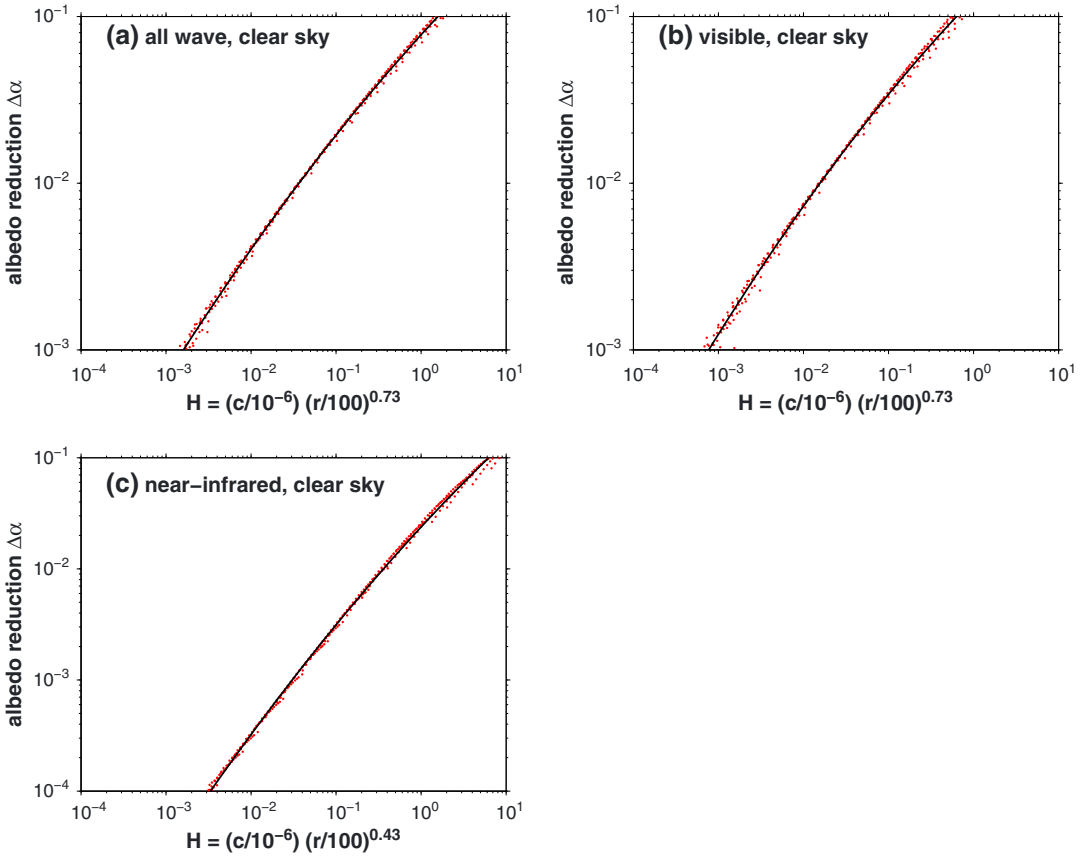

Figure 6. Combination of snow grain radius and BC content into a single predictor H for BC-induced albedo reduction (equation (7)). The points are DISORT results for snow grain sizes $r \geq 50$ μm; the curve is a quadratic fit to the points (Table 3).

Table 3. Simple Parameterization for $\Delta\alpha$, Combining r and C[a]

	m_1	m_2	m_3	s	Valid Range of H
			Clear Sky		
All-wave	−0.042	0.560	−1.110	0.73	$1.4\times10^{-3} < H < 1.6$
Visible	−0.049	0.525	−0.893	0.73	$6.9\times10^{-4} < H < 0.63$
Near-IR	−0.053	0.827	−1.623	0.43	$3.2\times10^{-3} < H < 6.3$
			Overcast Cloud		
All-wave	−0.043	0.547	−1.038	0.73	$1.1\times10^{-3} < H < 1.2$
Visible	−0.050	0.514	−0.890	0.73	$6.6\times10^{-4} < H < 0.79$
Near-IR	−0.050	0.832	−1.533	0.43	$2.5\times10^{-3} < H < 5.0$

[a]The snow grain radius r and BC mixing ratio C are combined into a single variable H (equation (7)) for computation of albedo reduction $\Delta\alpha$ (equation (8)). The exponent s for equation (7) and the coefficients m for equation (8) are given here. The parameterization is valid for grain radii 50–2500 μm.

consider Band 14 because the albedo of pure snow in that band is so small that adding BC to snow does not significantly affect the albedo. For Bands 7–13 the effect of r on $\Delta\alpha$ is not monotonic because for coarse-grained snow the albedo at these wavelengths is so low that it cannot be reduced much by BC; $\Delta\alpha$ therefore maximizes at an intermediate value of $r \approx 100$ μm and cannot be represented by the simple functions used in the parameterizations of Table 2. However, $\Delta\alpha$ is very small in these bands for values of C typically found in snow. Furthermore, Bands 7–13 are of minor importance for the surface energy budget; the fraction of incident solar flux at $\lambda > 1.24$ μm is only 12% for our clear-sky spectrum and 6% for our cloudy-sky spectrum. We therefore have not parameterized $\Delta\alpha$ for Bands 7–13. For Bands 2–6 we have developed parameterizations similar to those of Table 2; their coefficients are given in the supporting information.

6. Dust Characteristics for Modeling

Windblown mineral dust varies in composition depending on the source region. Several reports of its spectral absorption coefficient have been published for the spectral regions where snow albedo is sensitive to impurities (UV and visible). We will review these below, along with other relevant physical and optical properties of dust.

6.1. Sources of Dust

The largest dust source for the global atmosphere is Africa north of the equator, releasing ~800 megatons (Mt)/yr [*Formenti et al.*, 2011]. The second largest source is China-Mongolia (100–460 Mt/yr). However, their influence on snow is not proportionate to these numbers. Dust is carried by the atmosphere from central and southern Asia to the Himalayas and Pamirs, from Arizona to Colorado, and from Australia to New Zealand. But because most of the optical measurements of dust have come from studies of North African dust, our discussion is likewise focused there, and the values we will choose for our modeling are a modification of one of the Saharan measurements. In some studies the dust was sampled at various distances from the source, with some measurements made downwind across the Atlantic. We discuss these measurements below and consider whether they are appropriate for modeling dust in snow.

Table 4. Bands for the Rapid Radiative Transfer Model (RRTM) [*Mlawer and Clough*, 1997]

	Wavelength Boundaries (μm)	
Band Number	Low	High
1	0.2000	0.2632
2	0.2632	0.3448
3	0.3448	0.4415
4	0.4415	0.6250
5	0.6250	0.7782
6	0.7782	1.2422
7	1.2422	1.2987
8	1.2987	1.6260
9	1.6260	1.9417
10	1.9417	2.1505
11	2.1505	2.5000
12	2.5000	3.0769
13	3.0769	3.8462
14	3.8462	12.1951

Formenti et al. [2011] pointed out that dust from the Sahel (10°–20°N, e.g.,

Niger, Burkina Faso, and Mauritania) is redder and more absorptive than dust from the Sahara (20°–30°N), citing *Lazaro et al.* [2008]. *McConnell et al.* [2010] say "The content and speciation of iron oxides vary with source, with Sahelian sources being generally richer in absorbing iron oxides than the Saharan ones," citing *Formenti et al.* [2008] and *Claquin et al.* [1999]. Winter is the dry season in the Sahel, so the Sahel is a source of dust for the Atlantic only in winter. In summer the Sahel is wet, so summer dust measured in the Atlantic comes only from the Sahara. Regional differences within Africa therefore result in seasonal differences in absorption and redness of aerosol transported out over the Atlantic.

6.2. Dust Density

Reported densities for mineral dust are consistent with those of typical crustal minerals. Measured densities for atmospheric dust particles from the Sahara (in $\mathrm{kg\,m^{-3}}$) are 2500 [*Linke et al.,* 2006] or 2450–2700 [*Haywood et al.,* 2001]. Values of 2500 were used by *Zender et al.* [2003] and 2650 by *Haywood et al.* [2003]. A smaller value of 2000 was retrieved from mass closure by *Maring et al.* [2003]. We adopt $2500\,\mathrm{kg\,m^{-3}}$ for our modeling because it is in the middle of the reported values.

6.3. Dust Size Distribution

Measured size distributions of dust aerosol are commonly fitted to the sum of two or three lognormal modes, as was done, for example, by *Clarke et al.* [2004] for East Asian dust. We use a single lognormal size distribution for mineral dust, with geometric mean diameter $D_g = 0.65\,\mu\mathrm{m}$ and geometric standard deviation $\gamma_g = 2$ (see definitions in *Reist* [1993]). This distribution has mode diameter 0.4 μm and mass-mean diameter $D_{mm} = 3.5\,\mu\mathrm{m}$. This distribution is meant to represent a combination of modes 1 and 2 of the three-mode description for East Asian dust [*Clarke et al.,* 2004, Figure 5c]. Our D_{mm} of 3.5 μm is also in the middle of the range shown for dust undergoing long-range transport in a review of Saharan dust ("Coarse Mode 1" in *Formenti et al.* [2011, Figure 4]). The coarsest dust is found near sources [*Kok*, 2011; *Goudie and Middleton*, 2006, Table 6.8]. *Maring et al.* [2003] showed how the size distribution evolves with time, for Saharan dust sampled first near the Sahara in the Canary Islands and then later after traveling across the Atlantic to Puerto Rico. Our D_{mm} of 3.5 μm corresponds to a transport time of 4 days in Figure 5 of *Maring et al.* [2003]; after 10 days D_{mm} drops to 3.3. Since our principal results are for broadband albedos, we think that a single dust mode is adequate for modeling of snow albedo. The distribution we have chosen ($D_g = 0.65$; $\gamma_g = 2$) has $D_{mm} = 3.5\,\mu\mathrm{m}$, in line with observations of dust undergoing long-range transport, and it is consistent with other recent modeling efforts. The corresponding effective radius of the dust is 1.1 μm [*Reist*, 1993, equation (2.11)].

Snow often contains dust not only from long-range transport but also from the local soil, especially in semidesert areas with thin snow. We observed this on farmland in the Great Plains of North America [*Doherty et al.,* 2014], and in the rangeland of Inner Mongolia [*Huang et al.,* 2011], where hooves of grazing animals would kick soil onto nearby snow. This source of LAI is currently ignored by climate models, which consider only long-range transport when computing the dust content of snow. The soil and short-range-transported dust have sizes much larger than those described above; a size distribution measured in southwest Colorado [*Lawrence et al.,* 2010] found a peak of the volume distribution at a diameter of 50 μm. For our parameterization we are considering only long-range-transported dust, because that is what GCMs do, but we do think that it will be important in the future for climate models to consider these additional routes for incorporation of nearby soil into snow.

6.4. Complex Refractive Index of Dust

There is little disagreement about the real index m_{re}; it is 1.50–1.55 with only slight wavelength dependence [e.g., *Balkanski et al.,* 2007, Figure 4b]. The wavelength dependence of the imaginary index m_{im}, or alternatively the absorption coefficient k_{abs}, is more variable for different dust types. It has been inferred using a range of methods, with the resulting spectral indices shown in Figure 7. It varies with the type of dust, in particular with the content of the strongly absorbing iron oxides hematite and goethite. In our past work on dust in snow [*Warren and Wiscombe*, 1980] we used the spectral imaginary index reported for Saharan dust by *Patterson et al.* [1977, hereinafter PGS], which Warren and Wiscombe called "red dust." The PGS imaginary index is also in use by NCAR's Community Atmosphere Model version 4. However, there is recent evidence that much of the atmospheric mineral dust is less absorptive, and perhaps also

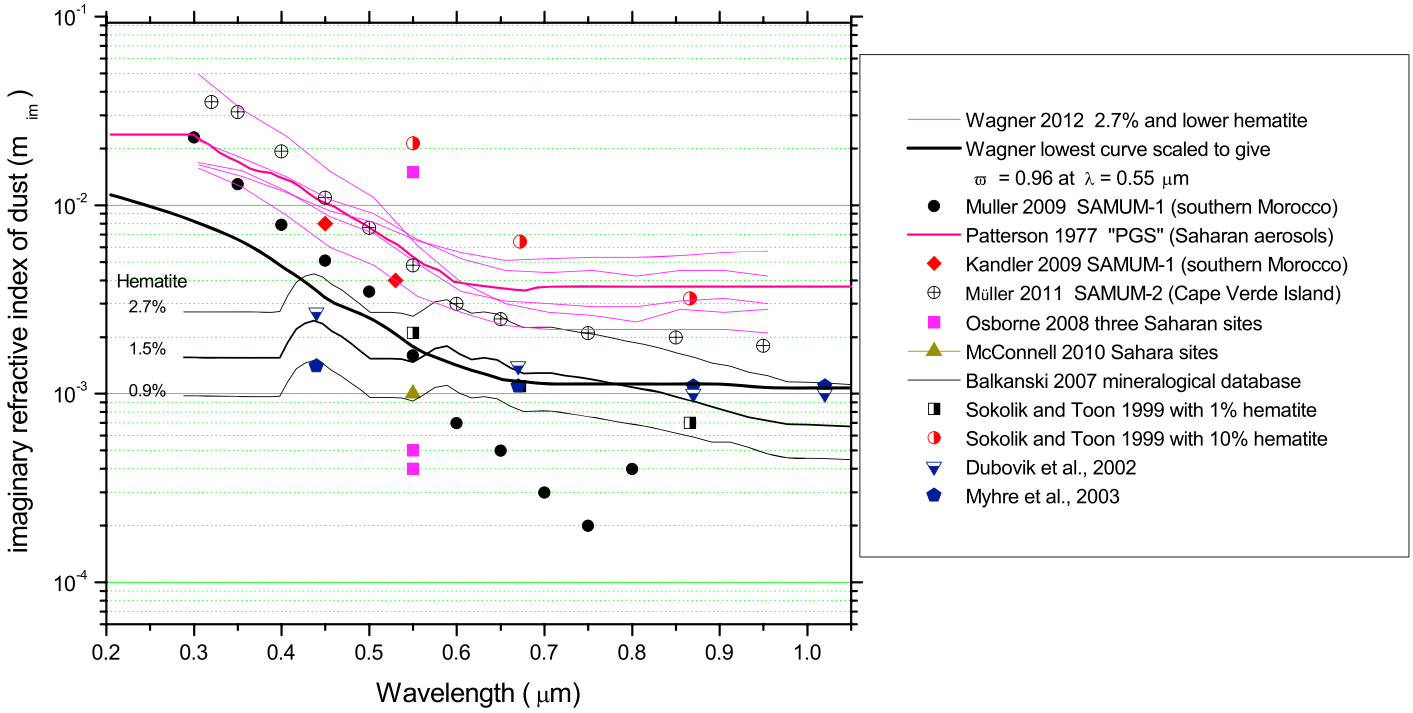

Figure 7. Spectral absorption coefficient of mineral dust, expressed as the imaginary part of the complex index of refraction (m_{im}), from field measurements at several locations discussed in the text. The bold blue curve is from *Patterson et al.* [1977] ("PGS"); it was used in our earlier modeling as "red dust" [*Warren and Wiscombe*, 1980]. The "Wagner lowest curve" [*Wagner et al.,* 2012] is also shown scaled down by a constant factor to obtain a single-scattering albedo $\varpi = 0.96$ at $\lambda = 550$ nm, resulting in the bold black curve, used for the computations in this paper. The extrapolation to longer and shorter wavelengths is based on the spectral behavior of hematite and goethite [*Sherman and Waite*, 1985].

less red, than PGS reported. The single-scattering albedo of PGS dust at wavelength 550 nm is $\varpi \approx 0.85$, whereas most atmospheric aerosol apparently has $\varpi \approx 0.96$ or even higher at 550 nm. In the ACE-Asia project, *Doherty et al.* [2005, Table 10] found $\varpi = 0.96$ for the size mode $D > 1$ μm at $\lambda = 550$ nm. *Lafon et al.* [2006] found that retrievals from the Aerosol Robotic Network (AERONET) imply midvisible $\varpi \geq 0.95$. In Morocco, *Kandler et al.* [2009] found $\varpi \approx 0.95$ at $\lambda = 550$ nm. *McConnell et al.* [2010] found values 0.97–0.98 over Mauritania. In Niger, *Osborne et al.* [2008] obtained $\varpi = 0.99$. For Saharan dust, *Haywood et al.* [2003] obtained ϖ between 0.95 and 0.99.

The spectral dependence of absorption can be described by the absorption Ångström exponent $Å_{abs}$ such that the mass absorption cross-section B_a is proportional to $\lambda^{-Å_{abs}}$ [e.g., *Grenfell et al.,* 2011, equation (8)]. The PGS dust has $Å_{abs} = 3.6$ for 450–600 nm. The review of *Sokolik et al.* [1993, Figure 1] showed PGS dust to have the steepest wavelength dependence of the reports they cited. Some recent reported values of Å are lower, but some are similar to PGS: $Å_{abs} = 2.34$ over the Atlantic [*Reid et al.,* 2003], 2.83 in Tunisia [*Alfaro et al.,* 2004], a median of 3.2 for pure dust in the Moroccan Sahara over the wavelength range 467–660 nm [*Petzold et al.,* 2009], and 2.2–4.5 for Saharan dust [*Müller et al.,* 2011]. In our snow sampling expeditions we have collected samples of the soil below the snow, because it can be a major source for LAI in the snow. Median values of Ångström exponents for soil were 3.66 in China [*Huang et al.,* 2011; *Wang et al.,* 2013] and 3.5–4.7 in western North America [*Doherty et al.,* 2014]. Soil, of course, contains organic material as well as mineral dust. Volcanic ash from the Antarctic Ice Sheet had $Å_{abs} = 3.13$ [*Dadic et al.,* 2013].

Most, but not all, of the recent measurements of m_{im} fall below that of PGS and show weaker wavelength dependence. Three studies that do agree with PGS are *Müller et al.* [2009], *Müller et al.* [2011], and *Wagner et al.* [2012, Figures 10 and 11]. The Wagner study was performed on dust generated in the laboratory by dispersing soil samples, including red soil from Burkina Faso.

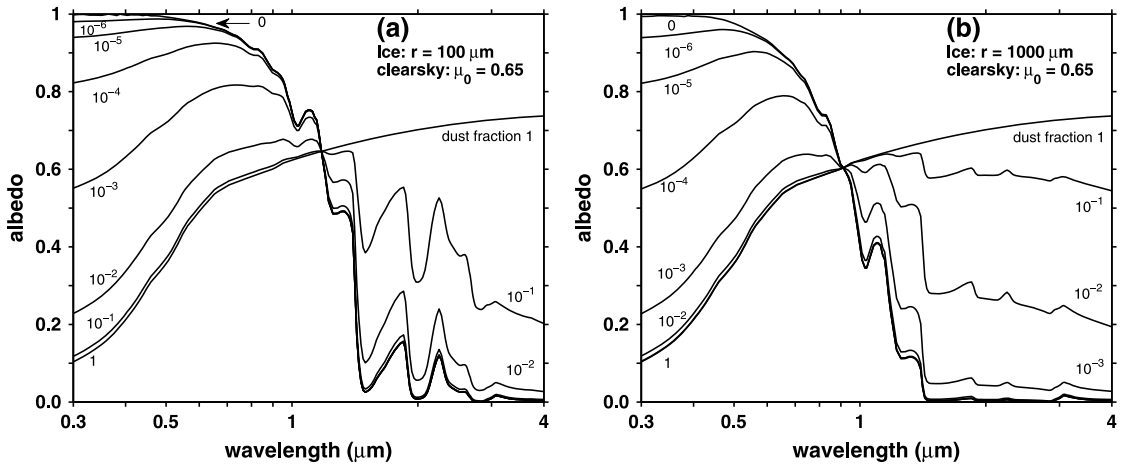

Figure 8. Spectral albedo of pure snow and of snow containing mineral dust at several mass fractions between 0 and 1. These computations use the dust absorption spectrum shown as the bold black curve in Figure 7. Snow grain radii (a) $r = 100\ \mu m$ and (b) $r = 1000\ \mu m$.

A number of recent studies have adopted values reported by *Balkanski et al.* [2007], so we explain here in some detail why we think they are not appropriate for our modeling. Some recent uses of those values were to explore the impact of different hematite/goethite mixes on optical properties [*Meland et al.,* 2011], to explain the impact of the optical properties of dust on aerosol retrievals [*Solmon et al.,* 2008] and to show consistency with other model simulations [e.g., *Zhao et al.,* 2011]. Balkanski et al. used laboratory-measured absorption spectra of pure minerals and combined them in different ways (using mixing rules) to determine which combination best matched measurements from the AERONET "over all sites where mineral dust is the dominant aerosol component." Other likely constituents of the aerosol include BC, which could explain their low value of $Å_{abs}$, since $Å_{abs}$ of BC is ~1.0 (Figure 3e). Balkanski et al. used hematite to represent the sum of hematite and goethite; the hump in m_{im} at 450 nm shown in Figure 7 is apparently the result of this choice: hematite has such a hump but goethite does not [*Sherman and Waite,* 1985, Figure 5]. Balkanski et al. obtained the best agreement with AERONET measurements when 1.5% hematite was internally mixed with other (mainly nonabsorbing) minerals (their Figure 4). They limited their comparison to the summer season (i.e., to the Sahara; see above) when $\varpi = 0.95$. They excluded the winter season when $\varpi = 0.86$, because they thought this meant there was a significant amount of BC in the aerosol. However, PGS dust has $\varpi = 0.86$ in midvisible, so an alternative explanation for the low winter ϖ would be that the source in winter is mostly Sahel, which has more-absorptive dust. In any case, by

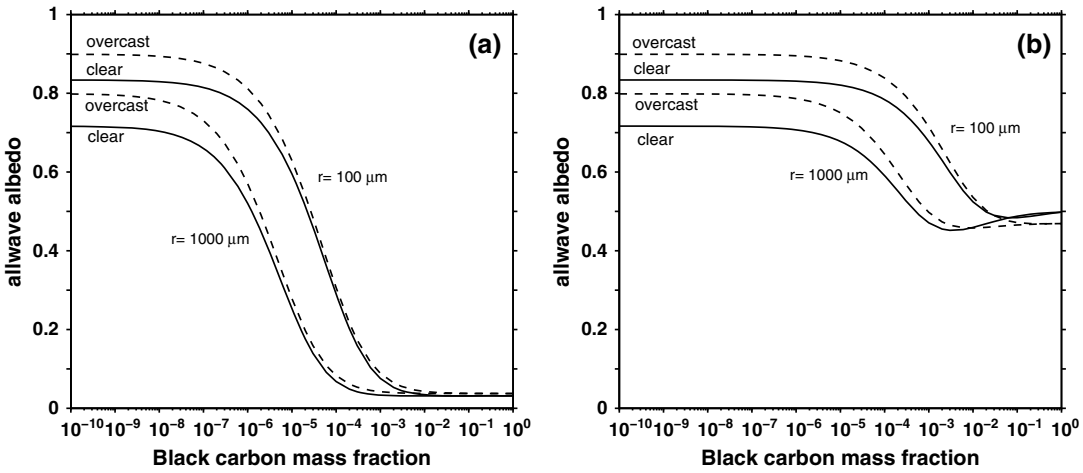

Figure 9. All-wave albedo as a function of the mass fraction of (a) BC or (b) dust, for two snow grain sizes ($r = 100$ and 1000 μm) and two incident solar spectra (clear sky and overcast sky). The plot for BC is an update of Figure 1 of *Warren and Wiscombe* [1985], using revised optical constants of ice and revised optical properties of BC.

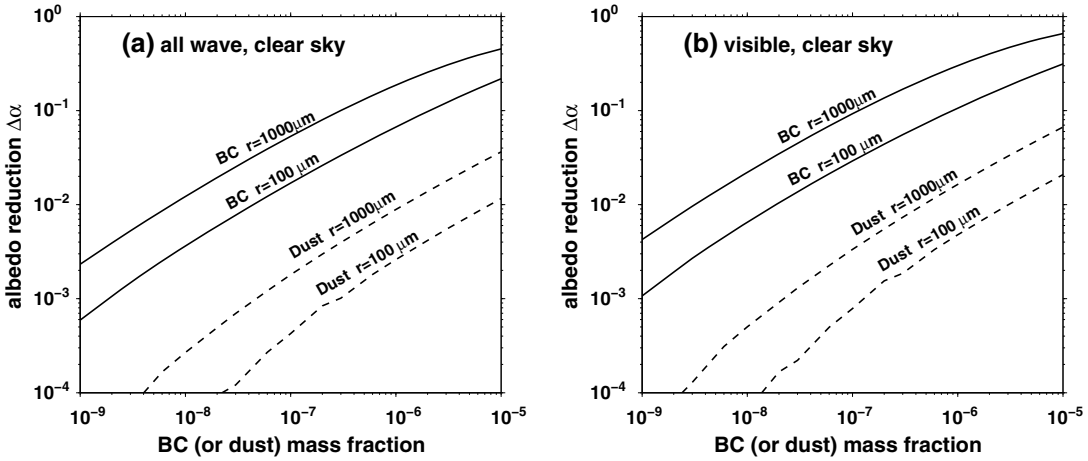

Figure 10. Comparison of albedo reduction by BC (as in Figure 5) and by dust. (a) All-wave and (b) visible. The BC equivalent of dust is determined by shifting the dust curves to the left until they align with the BC curves (Figure 11).

using only summertime data, Balkanski et al. have excluded the half of the year when the Sahel dominates the North African dust.

Figure 7 contains the three curves from Figure 4 of *Balkanski et al.* [2007], for hematite contents 0.9, 1.5, and 2.7%. These spectra have some peculiar characteristics:

1. They are flat from 300 to 400 nm then exhibit a hump between 400 and 500 nm.
2. Their absorption Ångström exponent from 400 to 600 nm is 1.0, the same as BC.
3. The three curves parallel each other, indicating that the hematite content has no influence on $Å_{abs}$. Aerosols with greater hematite content should be redder; i.e., have larger $Å_{abs}$, as was the case for dust with 1% and 10% hematite given by *Sokolik and Toon* [1999] (Figure 7).

The rationale for our choice of dust imaginary index $m_{im}(\lambda)$ is as follows. To obtain an Ångström exponent corresponding to most desert dust samples and also to obtain $\varpi = 0.96$ at $\lambda = 550$ nm to agree with the consensus of aircraft measurements of dust aerosol [e.g., *Doherty et al.,* 2005], we have taken the lowest curve of *Wagner et al.* [2012] and scaled it down at all wavelengths by a single factor to obtain $\varpi = 0.96$ at $\lambda = 550$ nm. This $m_{im}(\lambda)$, together with our dust size distribution, gives $B_a(\lambda)$ that has $Å_{abs} = 3.45$ from 400 to 600 nm wavelength (Figure 3e). This curve (the bold black curve in Figure 7) is essentially parallel to that of PGS but lower by a factor of ~3.

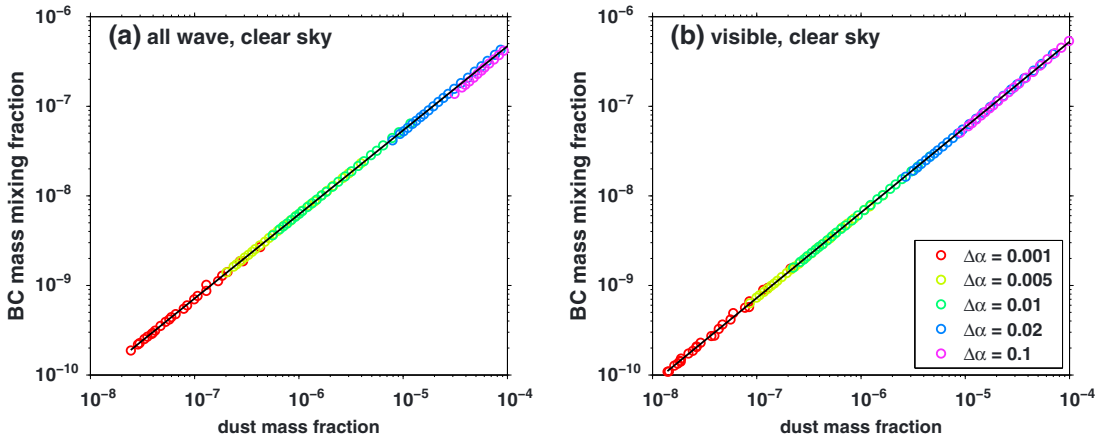

Figure 11. Mass fraction of BC needed to obtain the same $\Delta\alpha$ resulting from a given mass fraction of dust. Each point is for a particular value of $\Delta\alpha$. (a) All-wave and (b) visible.

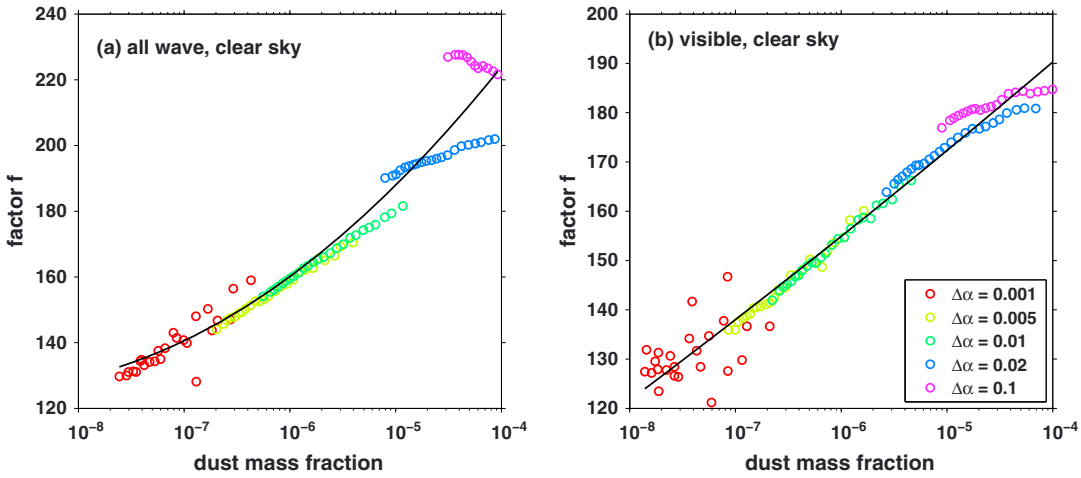

Figure 12. Factor f by which the dust mass fraction (C_d) must be divided to obtain its BC equivalent, as a function of dust mass fraction, for several values of $\Delta\alpha$. The solid curve is used to parameterize f as a function of C_d.

7. Single-Scattering by Mineral Dust Particles

Single-scattering results for dust with the above specifications are shown in Figure 3. The single-scattering albedo of dust is much higher than that of BC, but the effect of scattering by dust on snow albedo is negligible except at very large dust mass fractions, because the scattering by snow grains is dominant. It is the absorption properties of dust that are relevant, and Figure 3e shows that B_a for dust is 2 orders of magnitude smaller than B_a for BC. However, in part because of its larger particle size, the mass of dust in snow can also be orders of magnitude larger than the mass of BC, making its contribution to albedo reduction comparable to or greater than that of BC [*Painter et al.,* 2007; *Wang et al.,* 2013; *Doherty et al.,* 2014].

8. Albedo Reduction by Dust in Snow

Figure 8 shows the effect on spectral albedo of adding dust to snow, in mass fractions from 10^{-6} to 10^{-1}, as well as the end-member spectra for pure snow and pure dust. These plots may be compared to the similar plots for BC in snow shown in Figure 4. The spectral albedo of dust is approximately opposite to that of snow, in that the albedo for pure dust is low at visible and UV wavelengths and higher in the near-IR. The curves in Figure 8a all cross at $\lambda = 1.2\,\mu$m, where the albedo of pure dust equals the albedo of pure snow at a value $\alpha_\lambda = 0.64$. The wavelength of this cross point varies with snow grain size; for $r = 1000\,\mu$m the curves cross at $\lambda = 0.9\,\mu$m, $\alpha_\lambda = 0.60$ (Figure 8b). As was also seen for BC, a given mass fraction of dust causes a greater reduction of albedo in coarse-grained snow than in fine-grained snow (compare Figure 8b to Figure 8a). In Figure 9b, the asymptote for pure dust gives an albedo of 0.5, somewhat higher than that of desert surfaces [*Smith*, 1986; *Otterman and Fraser*, 1976], probably because airborne dust has a smaller particle size than surface soil.

Table 5. Parameterization of the Factor f as a Function of Dust Mass Fraction[a]

	v_0	v_1	v_2
		Clear Sky	
All-wave	159	23.94	4.30
Visible	155	17.15	0.27
		Overcast Sky	
All-wave	155	20.97	2.41
Visible	152	15.92	−0.39

[a]To compute albedo reduction for the all-wave and visible bands, the dust mass fraction C_d is converted into BC-equivalent mass fraction by dividing by the factor f, which is a function of C_d. The factor f is obtained from equation (10) with coefficients listed here.

The all-wave albedo as a function of the mass fraction of BC or dust is shown in Figures 9a and 9b, respectively. Three of the curves in Figure 9b show a weak minimum of albedo for dust mass fractions between 10^{-3} and 10^{-1}, depending on snow grain size. This peculiarity is a consequence of the spectral contrast of ice and dust particles (Figure 8); it is not seen with

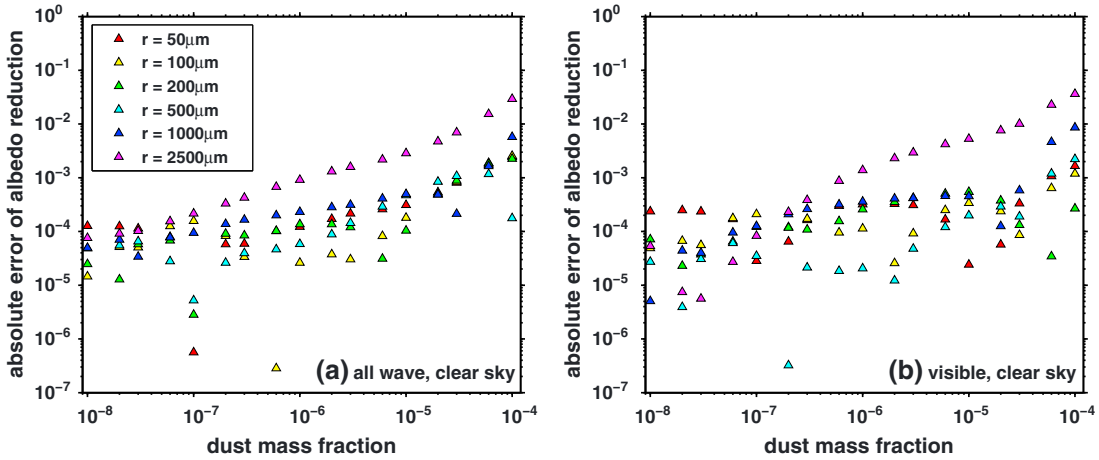

Figure 13. Error in $\Delta\alpha$ resulting from approximating C_d as the equivalent mass fraction of C_{BC}, as given by the solid curves from Figure 12.

BC (Figure 9a). At these dust fractions, dust begins to affect the albedo not only by absorption but also by scattering, and by limiting the penetration depth of radiation into the snowpack.

Comparing Figures 9a and 9b, it is apparent that for dust mass fractions $C_d \leq 10^{-4}$, the dust curves can match the BC curves if the dust curves are shifted to the left by a factor $f \approx 200$. Thus, for all-wave albedo the effect of dust can be mimicked by BC at a mass fraction ~0.5% as large. BC and dust mass fractions can therefore be combined into an "equivalent BC" mass fraction. Using the terminology of *Grenfell et al.* [2011], the BC-equivalent mass fraction, C_{BC}^{eq}, is given by

$$C_{BC}^{eq} = C_{BC} + C_d/f. \tag{9}$$

The factor f varies with C_d, so we now investigate how to express this dependence. Figure 10 compares $\Delta\alpha$ for BC and dust for mass fractions $<10^{-5}$. We show results only for visible and all-wave, because dust in these amounts causes little change to the broadband near-IR albedo. (At a mass fraction of 10^{-5}, the near-IR $\Delta\alpha$ does not exceed 0.002; even at a mass fraction of 10^{-4}, $\Delta\alpha$ does not exceed 0.01.) As mentioned above, this is because the near-IR albedo of pure dust is close to that of pure snow.

We now ask how far to the left a point on the dashed curves (dust) of Figure 10 must be moved to reach the solid curves (BC). The result of this exercise is shown in Figure 11, a curve about 2 orders of magnitude below the 1:1 line, but with a slope smaller than 1:1, implying that f increases with C_d. Figure 12 plots f as a function

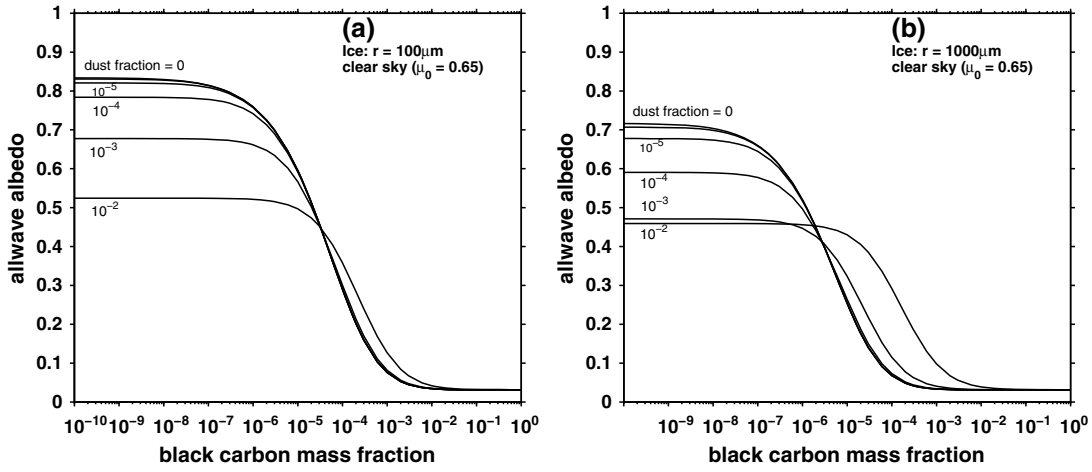

Figure 14. The combined effect of dust and BC on all-wave albedo, as a function of BC mass fraction, for snow containing dust at several mass fractions. Snow grain radii (a) $r = 100$ μm and (b) $r = 1000$ μm.

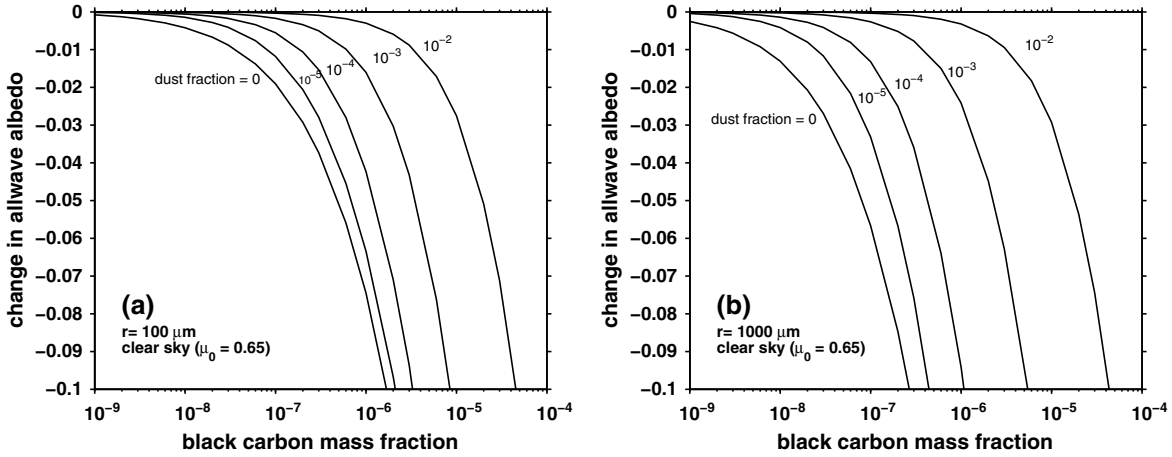

Figure 15. Change in all-wave albedo due to addition of BC to already-dusty snow, as a function of BC mass fraction. Snow grain radii (a) $r = 100\,\mu m$ and (b) $r = 1000\,\mu m$.

of C_d for dust mass fraction $\leq 10^{-4}$. The quadratic fits (solid curves) can be used to calculate the factor f as a function of C_d. Define $x \equiv \log_{10}$ [C_d (ppm)]. Then

$$f = v_0 + v_1 x + v_2 x^2. \tag{10}$$

The coefficients are given in Table 5.

For all-wave albedo at large C_d (Figure 12a), the curve is a poor fit to the data. However, we must remember that our aim is to obtain accuracy not in f but rather in $\Delta\alpha$, and it turns out that $\Delta\alpha$ is not very sensitive to f in this range. The error in calculated albedo reduction caused by representing dust as an equivalent BC ranges from 10^{-5} to 3×10^{-2}, depending on the dust mass fraction and snow grain size (Figure 13). For $r \leq 1000\,\mu m$ the error does not exceed 0.01. More figures related to the estimation and evaluation of the factor f are included in the supporting information.

9. Combinations of Dust and BC

If BC and dust are both present at low mixing ratios, e.g., 10 ng/g, their effects in reducing snow albedo are just additive ($\Delta\alpha \approx \Delta\alpha_{dust} + \Delta\alpha_{BC}$), but for larger mixing ratios $\Delta\alpha < \Delta\alpha_{dust} + \Delta\alpha_{BC}$. Computations of the potential benefits of reducing BC emissions must therefore account for the presence of dust and soil loading in snow. Dust content can be quite high in mountain glaciers. For example, in the Himalaya, *Ming et al.* [2013] and *Kaspari et al.* [2014] reported that the effect of BC was notably muted because of the high dust content.

Figure 14 shows the all-wave albedo of dust-laden snow as a function of added BC, and Figure 15 shows the reduction of all-wave albedo by BC for several preexisting dust contents in the snow. A related figure on this same topic was shown by *Bond et al.* [2013] as their Figure 30.

10. Summary

The broadband albedo of pure deep snow can be represented by a simple quadratic function of grain size, which can also incorporate the influence of solar zenith angle. However, natural snow usually contains sufficient impurities to significantly affect the albedo. Black carbon mixing ratios in snow, remote from sources of pollution, vary over 4 orders of magnitude. Here we have parameterized the reduction of broadband snow albedo ($\Delta\alpha$) due to BC in these amounts, using a quadratic or cubic polynomial in BC mixing ratio, whose coefficients are themselves quadratic in snow grain size. We also have combined grain size and BC into a single predictor for a much simpler parameterization of $\Delta\alpha$, but with the allowable grain radius domain limited to $r \geq 50\,\mu m$. For reduction of visible albedo, we have shown that the effect of mineral dust on snow albedo can be represented, via a divisor, by using an "equivalent" BC

mixing ratio. The addition of mineral dust to snow does not significantly change the broadband albedo for the near-IR band (0.7–4.0 μm), because the absorption properties of dust grains and snow grains are similar when averaged over this wavelength domain.

The model calculations on which the parameterizations are based required assumptions about the size distributions and complex refractive indices for the particulate impurities. The parameterizations can be used for BC and dust of different sizes and refractive indices by scaling the mass mixing ratio in the parameterization according to the ratios of their spectral mass absorption cross-section B_a (Figure 3e).

Appendix A: Combining Single-Scattering Quantities for Ice, Dust, and Black Carbon

We combine the single-scattering properties of up to three particulate components present as an external mixture; i.e., the scattering and absorption properties of dust and BC particles are computed assuming they are isolated from the snow grains, not located inside the snow grains.

Snow consists of a mixture of ice, dust, BC, and air, with size distributions of the particulate components $n_i(r_i)$, $n_j(r_j)$, and $n_k(r_k)$, respectively; units of n are particles per m^3. A single ice particle (assumed spherical) has volume $V_i = \frac{4}{3}\pi r_i^3$ and cross-section area $A_i = \pi r_i^2$, similarly for a dust particle with volume V_j and area A_j and a BC particle with volume V_k and area A_k. If the n values are accurately scaled using scale factors f_i as defined below, then the density of snow (units $\mathrm{kg\,m^{-3}}$) is

$$\rho_{\mathrm{snow}} = f_{\mathrm{ice}}\rho_{\mathrm{ice}}\sum_i V_i n_i + f_{\mathrm{dust}}\rho_{\mathrm{dust}}\sum_j V_j n_j + f_{\mathrm{BC}}\rho_{\mathrm{BC}}\sum_k V_k n_k, \tag{A1}$$

where $\rho_{\mathrm{ice}} = 917\ \mathrm{kg\,m^{-3}}$, $\rho_{\mathrm{dust}} = 2500\ \mathrm{kg\,m^{-3}}$, and $\rho_{\mathrm{BC}} = 1800\ \mathrm{kg\,m^{-3}}$.

In practice, each of these three size distributions would usually have been obtained separately with arbitrary normalization, so they must be rescaled for each new set of mass fractions (C_{dust} and C_{BC}), using the scaling factors f_{ice}, f_{dust}, and f_{BC}, as given below, assuming that ρ_{snow} is specified.

Abbreviating Q_{ext} as simply Q, the extinction efficiencies are Q_i, Q_j, and Q_k, for ice, dust, and BC, respectively. For ice the extinction cross-section area per unit volume (units m^2/m^3) is

$$\sigma_{\mathrm{ext}}^{\mathrm{ice}} = f_{\mathrm{ice}}\sum_i Q_i A_i n_i, \tag{A2}$$

and the scattering cross-section area per unit volume is

$$\sigma_{\mathrm{sca}}^{\mathrm{ice}} = f_{\mathrm{ice}}\sum_i Q_i A_i \varpi_i n_i. \tag{A3}$$

The single-scattering albedo for the size distribution of snow grains is

$$\varpi_{\mathrm{ice}} = \sigma_{\mathrm{sca}}^{\mathrm{ice}}/\sigma_{\mathrm{ext}}^{\mathrm{ice}}. \tag{A4}$$

The asymmetry parameter for the size distribution is

$$g_{\mathrm{ice}} = \frac{f_{\mathrm{ice}}\sum_i g_i Q_i A_i \varpi_i n_i}{f_{\mathrm{ice}}\sum_i Q_i A_i \varpi_i n_i} = \frac{f_{\mathrm{ice}}\sum_i g_i Q_i A_i \varpi_i n_i}{\sigma_{\mathrm{sca}}^{\mathrm{ice}}}. \tag{A5}$$

Similar relations give the corresponding quantities for dust and BC:

$$\sigma_{\mathrm{sca}}^{\mathrm{dust}}, \sigma_{\mathrm{ext}}^{\mathrm{dust}}, g_{\mathrm{dust}}, \sigma_{\mathrm{sca}}^{\mathrm{BC}}, \sigma_{\mathrm{ext}}^{\mathrm{BC}}, g_{\mathrm{BC}}.$$

The mass absorption cross section for example for dust (units m^2/kg) is

$$B_a = \frac{\sigma_{\mathrm{ext}}^{\mathrm{dust}} - \sigma_{\mathrm{sca}}^{\mathrm{dust}}}{f_{\mathrm{ice}}\rho_{\mathrm{dust}}\sum_j V_j n_j}. \tag{A6}$$

If Q and ϖ are the same for all the dust particles (as they would be for a monodispersion), equation (A6) reduces to

$$B_a = \frac{3Q(1-\varpi)}{4r_{\text{eff}}\rho_{\text{dust}}}, \tag{A7}$$

where the effective radius [*Hansen and Travis*, 1974] is

$$r_{\text{eff}} = \frac{\sum_j r_j^3 n_j}{\sum_j r_j^2 n_j}. \tag{A8}$$

Equation (A7) is the same as equation (6) in the main paper.

For a medium consisting of a mixture of air with just one particulate component (ice, dust, or BC), equations A2, A3, A4, A5, A6 are appropriate. For a multicomponent mixture the following equations apply.

Define the mass fractions of ice, dust, and BC as C_{ice}, C_{dust}, and C_{BC}. Ignoring the negligible mass of air, the mass fractions of the particles add to 1:

$$C_{\text{ice}} + C_{\text{dust}} + C_{\text{BC}} = 1. \tag{A9}$$

The scaling factors for the ice, dust, and BC size distributions, needed below, are (from equation (A1))

$$f_{\text{ice}} = \frac{C_{\text{ice}}\rho_{\text{snow}}}{\rho_{\text{ice}}\sum_i V_i n_i}. \tag{A10}$$

$$f_{\text{dust}} = \frac{C_{\text{dust}}\rho_{\text{snow}}}{\rho_{\text{dust}}\sum_j V_j n_j}; \tag{A11}$$

$$f_{\text{BC}} = \frac{C_{\text{BC}}\rho_{\text{snow}}}{\rho_{\text{BC}}\sum_k V_k n_k}; \tag{A12}$$

The extinction cross section for the mixture is

$$\sigma_{\text{ext}} = f_{\text{dust}}\sigma_{\text{ext}}^{\text{dust}} + f_{\text{BC}}\sigma_{\text{ext}}^{\text{BC}} + f_{\text{ice}}\sigma_{\text{ext}}^{\text{ice}}. \tag{A13}$$

The optical depth of a layer of thickness Δz is

$$\tau = \sigma_{\text{ext}}\Delta z. \tag{A14}$$

The scattering cross section is

$$\sigma_{\text{sca}} = f_{\text{dust}}\sigma_{\text{sca}}^{\text{dust}} + f_{\text{BC}}\sigma_{\text{sca}}^{\text{BC}} + f_{\text{ice}}\sigma_{\text{sca}}^{\text{ice}}. \tag{A15}$$

The single-scattering albedo is

$$\varpi = \sigma_{\text{sca}}/\sigma_{\text{ext}}. \tag{A16}$$

The asymmetry parameter is

$$g = \left[g_{\text{ice}}f_{\text{ice}}\sigma_{\text{sca}}^{\text{ice}} + g_{\text{dust}}f_{\text{dust}}\sigma_{\text{sca}}^{\text{dust}} + g_{\text{BC}}f_{\text{BC}}\sigma_{\text{sca}}^{\text{BC}}\right]/\sigma_{\text{sca}}. \tag{A17}$$

If single-scattering quantities for pure snow have been precomputed, then the ice size distribution $n_i(r_i)$ is not needed; one can instead use C_i together with previously obtained values of ϖ_i, g_i, and $Q_{\text{ext}}^{\text{ice}}$. So in this case, from $Q_{\text{ext}}^{\text{ice}}$ one would compute $\sigma_{\text{ext}}^{\text{ice}}$ as

$$\sigma_{\text{ext}}^{\text{ice}} = \frac{3Q_{\text{ext}}^{\text{ice}}\rho_{\text{snow}}}{4r_{\text{eff}}\rho_{\text{ice}}}\left(\text{units } \text{m}^{-1}\right). \tag{A18}$$

In a "pure" snowpack (no dust or BC) we would have

$$\sum_i V_i n_i = \frac{\rho_{\text{snow}}}{\rho_{\text{ice}}} \quad (\text{from equation (A1)})$$

and $\sigma_{\text{ext}} = f_{\text{ice}}\sigma_{\text{ext}}^{\text{ice}}$ (from equation (A13)).

Then (A10) can be replaced by $f_{ice} = C_{ice}$. Alternatively, one can replace the third term in (A13), which is $f_{ice}\sigma_{ext}^{ice}$, by $\frac{3Q_{ext}^{ice}\rho_{snow}C_{ice}}{4r_{eff}\rho_{ice}}$. Note that the product $\rho_{snow}C_{ice}$ is the density the snowpack would have if all the dust and BC were removed from it.

Acknowledgments
We thank Tom Grenfell for providing digital values of the measured solar spectra and Yves Balkanski for digital values from his published figures. We thank Sarah Doherty, Dean Hegg, Tony Clarke, Dorothy Koch, Qiang Fu, Charlie Zender, Steve Hudson, Tom Ackerman, and Cecilia Bitz for their helpful discussion. We thank Sarah Doherty for her comments on an early draft and Tom Painter for his review. The research was supported by NSF grant AGS-11-18460. The data are available at the following website: http://www.atmos.washington.edu/articles/Snow_Albedo_Parameterization.

References

Ackerman, T. P., and O. B. Toon (1981), Absorption of visible radiation in atmosphere containing mixtures of absorbing and nonabsorbing particles, *Appl. Opt.*, *20*, 3661–3668.

Alfaro, S. C., S. Lafon, L. Rajot, P. Formenti, A. Gaudichet, and M. Maille (2004), Iron oxides and light absorption by pure desert dust: An experiment study, *J. Geophys. Res.*, *109*, D08208, doi:10.1029/2003JD004374.

Aoki, T., K. Kuchiki, M. Niwano, Y. Kodama, M. Hosaka, and T. Tanaka (2011), Physically based snow albedo model for calculating broadband albedos and the solar heating profile in snowpack for general circulation models, *J. Geophys. Res.*, *116*, D11114, doi:10.1029/2010JD015507.

Balkanski, Y., M. Schulz, T. Claquin, and S. Guibert (2007), Reevaluation of mineral aerosol radiative forcings suggests a better agreement with satellite and AERONET data, *Atmos. Chem. Phys.*, *7*, 81–95.

Beine, H., C. Anastasio, G. Esposito, K. Patten, E. Wilkening, F. Domine, D. Voisin, M. Barret, S. Houdier, and S. Hall (2011), Soluble, light-absorbing species in snow at Barrow, Alaska, *J. Geophys. Res.*, *116*, D00R05, doi:10.1029/2011JD016181.

Bond, T. C., and R. W. Bergstrom (2006), Light absorption by carbonaceous particles: An investigative review, *Aerosol Sci. Technol.*, *40*, 27–67.

Bond, T. C., et al. (2013), Bounding the role of black carbon in the climate system: A scientific assessment, *J. Geophys. Res. Atmos.*, *118*, 5380–5552, doi:10.1002/jgrd.50171.

Brandt, R. E., S. G. Warren, and A. D. Clarke (2011), A controlled snowmaking experiment testing the relation between black carbon content and reduction of snow albedo, *J. Geophys. Res.*, *116*, D08109, doi:10.1029/2010JD015330.

Claquin, T., M. Schulz, and Y. J. Balkanski (1999), Modeling the mineralogy of atmospheric dust sources, *J. Geophys. Res.*, *104*, 22,243–22,256, doi:10.1029/1999JD900416.

Clarke, A. D., and K. J. Noone (1985), Soot in the Arctic snowpack: A cause for perturbations in radiative transfer, *Atmos. Environ.*, *19*, 2045–2053.

Clarke, A. D., K. J. Noone, J. Heintzenberg, S. G. Warren, and D. S. Covert (1987), Aerosol light absorption measurement techniques: Analysis and intercomparisons, *Atmos. Environ.*, *21*, 1455–1465.

Clarke, A. D., et al. (2004), Size distributions and mixtures of dust and black carbon aerosol in Asian outflow: Physiochemistry and optical properties, *J. Geophys. Res.*, *109*, D15S09, doi:10.1029/2003JD004378.

Dadic, R., P. C. Mullen, M. Schneebeli, R. E. Brandt, and S. G. Warren (2013), Effects of bubbles, cracks, and volcanic tephra on the spectral albedo of bare ice near the Trans-Antarctic Mountains: Implications for sea glaciers on Snowball Earth, *J. Geophys. Res. Earth Surf.*, *118*, 1658–1676, doi:10.1002/jgrf.20098.

Dang, C., and D. A. Hegg (2014), Quantifying light absorption by organic carbon in Western North American snow by serial chemical extractions, *J. Geophys. Res. Atmos.*, *119*, 10,247–10,261, doi:10.1002/2014JD022156.

Doherty, S. J., P. K. Quinn, A. Jefferson, C. M. Carrico, T. L. Anderson, and D. Hegg (2005), A comparison and summary of aerosol optical properties as observed in situ from aircraft, ship, and land during ACE-Asia, *J. Geophys. Res.*, *110,* D04201, doi:10.1029/2004JD004964.

Doherty, S. J., S. G. Warren, T. C. Grenfell, A. D. Clarke, and R. E. Brandt (2010), Light-absorbing impurities in Arctic snow, *Atmos. Chem. Phys.*, *10*, 11,647–11,680.

Doherty, S. J., T. C. Grenfell, S. Forsström, D. L. Hegg, R. E. Brandt, and S. G. Warren (2013), Observed vertical redistribution of black carbon and other insoluble light-absorbing particles in melting snow, *J. Geophys. Res. Atmos.*, *118*, 5553–5569, doi:10.1002/jgrd.50235.

Doherty, S. J., C. Dang, D. A. Hegg, R. Zhang, and S. G. Warren (2014), Black carbon and other light-absorbing particles in snow of central North America, *J. Geophys. Res. Atmos.*, *119*, 12,807–12,831, doi:10.1002/2014JD022350.

Dubovik, O., B. Holben, T. F. Eck, A. Smirnov, Y. J. Kaufman, M. D. King, D. Tanré, and I. Slutsker (2002), Variability of absorption and optical properties of key aerosol types observed in worldwide locations, *J. Atmos. Sci.*, *59*, 590–608.

Flanner, M. G., C. S. Zender, J. T. Randerson, and P. J. Rasch (2007), Present-day climate forcing and response from black carbon in snow, *J. Geophys. Res.*, *112,* D11202, doi:10.1029/2006JD008003.

Flanner, M. G., C. S. Zender, P. G. Hess, N. M. Mahowald, T. H. Painter, V. Ramanathan, and P. J. Rasch (2009), Springtime warming and reduced snow cover from carbonaceous particles, *Atmos. Chem. Phys.*, *9*, 2481–2497.

Flanner, M. G., X. Liu, C. Zhou, J. E. Penner, and C. Jiao (2012), Enhanced solar energy absorption by internally-mixed black carbon in snow grains, *Atmos. Chem. Phys.*, *12*, 4699–4721.

Formenti, P., et al. (2008), Regional variability of the composition of mineral dust from western Africa: Results from the AMMA SOP0/DABEX and DODO field campaigns, *J. Geophys. Res.*, *113*, D00C13, doi:10.1029/2008JD009903.

Formenti, P., L. Schütz, Y. Balkanski, K. Desboeufs, M. Ebert, K. Kandler, A. Petzold, D. Scheuvens, S. Weinbruch, and D. Zhang (2011), Recent progress in understanding physical and chemical properties of African and Asian mineral dust, *Atmos. Chem. Phys.*, *11*, 8231–8256.

Forsström, S., J. Ström, C. A. Pedersen, E. Isaksson, and S. Gerland (2009), Elemental carbon distribution in Svalbard snow, *J. Geophys. Res.*, *114*, D19112, doi:10.1029/2008JD011480.

Fuller, K. A., W. C. Malm, and S. M. Kreidenweis (1999), Effects of mixing on extinction by carbonaceous particles, *J. Geophys. Res.*, *104*, 15,941–15,954, doi:10.1029/1998JD100069.

Gardner, A. S., and M. J. Sharp (2010), A review of snow and ice albedo and the development of a new physically based broadband albedo parameterization, *J. Geophys. Res.*, *115,* F01009, doi:10.1029/2009JF001444.

Goudie, A. S., and N. J. Middleton (2006), *Desert Dust in the Global System*, Springer, Heidelberg.

Grenfell, T. C., and D. K. Perovich (2008), Incident spectral irradiance in the Arctic Basin during the summer and fall, *J. Geophys. Res.*, *113*, D12117, doi:10.1029/2007JD009418.

Grenfell, T. C., and S. G. Warren (1999), Representation of a nonspherical ice particle by a collection of independent spheres for scattering and absorption of radiation, *J. Geophys. Res.*, *104*, 31,697–31,709, doi:10.1029/1999JD900496.

Grenfell, T. C., S. G. Warren, and P. C. Mullen (1994), Reflection of solar radiation by the Antarctic snow surface at ultraviolet, visible, and near-infrared wavelengths, *J. Geophys. Res.*, *99*, 18,669–18,684, doi:10.1029/94JD01484.

Grenfell, T. C., S. P. Neshyba, and S. G. Warren (2005), Representation of a nonspherical ice particle by a collection of independent spheres for scattering and absorption of radiation: 3. Hollow columns and plates, *J. Geophys. Res.*, *110,* D17203, doi:10.1029/2005JD005811.

Grenfell, T. C., S. J. Doherty, A. D. Clarke, and S. G. Warren (2011), Light absorption from particulate impurities in snow and ice determined by spectrophotometric analysis of filters, *Appl. Opt.*, *50*, 2037–2048.
Hadley, O. L., and T. W. Kirchstetter (2012), Black carbon reduction of snow albedo, *Nat. Clim. Change*, *2*, 437–440.
Hagler, G. S. W., M. H. Bergin, E. A. Smith, and J. E. Dibb (2007), A summer time series of particulate carbon in the air and snow at Summit, Greenland, *J. Geophys. Res.*, *112*, D21309, doi:10.1029/2007JD008993.
Hansen, J. E., and L. Nazarenko (2004), Soot climate forcing via snow and ice albedos, *Proc. Natl. Acad. Sci. U.S.A.*, *101*, 423–428.
Hansen, J. E., and L. D. Travis (1974), Light scattering in planetary atmospheres, *Space Sci. Rev.*, *16*, 527–610.
Haywood, J., P. Francis, S. Osborne, M. Glew, N. Loeb, E. Highwood, D. Tanré, G. Myhre, P. Formenti, and E. Hirst (2003), Radiative properties and direct radiative effect of Saharan dust measured by the C-130 aircraft during SHADE: 1. Solar spectrum, *J. Geophys. Res., 108*(D18), 8577, doi:10.1029/2002JD002687.
Haywood, J. M., P. N. Francis, M. D. Glew, and J. P. Taylor (2001), Optical properties and direct radiative effect of Saharan dust: A case study of two Saharan dust outbreaks using aircraft data, *J. Geophys. Res.*, *106*, 18,417–18,430, doi:10.1029/2000JD900319.
Hegg, D. A., S. G. Warren, T. C. Grenfell, S. J. Doherty, and A. D. Clarke (2010), Sources of light-absorbing aerosol in Arctic snow and their seasonal variation, *Atmos. Chem. Phys.*, *10*, 10,923–10,938.
Holland, M. M., D. A. Bailey, B. P. Briegleb, B. Light, and E. Hunke (2012), Improved sea ice shortwave radiation physics in CCSM4: The impact of melt ponds and aerosols on Arctic sea ice, *J. Clim.*, doi:10.1175/JCLI-D-11-00078.1.
Huang, J., Q. Fu, W. Zhang, X. Wang, R. Zhang, H. Ye, and S. Warren (2011), Dust and black carbon in seasonal snow across northern China, *Bull. Am. Meteorol. Soc.*, *92*, 175–181.
Jacobson, M. Z. (2004), Climate response of fossil fuel and biofuel soot, accounting for soot's feedback to snow and sea ice albedo and emissivity, *J. Geophys. Res.*, *109*, D21201, doi:10.1029/2004JD004945.
Kandler, K., et al. (2009), Size distribution, mass concentration, chemical and mineralogical composition and derived optical parameters of the boundary layer aerosol at Tinfou, Morocco, during SAMUM 2006, *Tellus, Ser. B*, *61*, 32–50.
Kaspari, S., T. H. Painter, M. Gysel, M. Schwikowski, and S. M. Skiles (2014), Seasonal and elevational variations of black carbon and dust in snow and ice in the Solu-Khumbu, Nepal and estimated radiative forcings, *Atmos. Chem. Phys.*, *14*, 8089–8103, doi:10.5194/acp-14-8089-2014.
Koch, D., S. Menon, A. DelGenio, R. Ruedy, I. Alienov, and G. A. Schmidt (2009), Distinguishing aerosol impacts on climate over the past century, *J. Clim.*, *22*, 2659–2677, doi:10.1175/2008JCLI2573.1.
Kok, J. F. (2011), A scaling theory for the size distribution of emitted dust aerosols suggests climate models underestimate the size of the global dust cycle, *Proc. Natl. Acad. Sci. U.S.A.*, *108*, 1016–1021.
LaChapelle, E. R. (1969), *Field Guide to Snow Crystals*, Univ. of Washington Press, Seattle.
Lafon, S., I. N. Sokolik, J. L. Rajot, S. Caquineau, and A. Gaudichet (2006), Characterization of iron oxides in mineral dust aerosols: Implications for light absorption, *J. Geophys. Res.*, *111*, D21207, doi:10.1029/2005JD007016.
Lawrence, C. R., T. H. Painter, C. C. Landry, and J. C. Neff (2010), The contemporary physical and chemical composition of aeolian dust deposition to terrestrial ecosystems of the San Juan Mountains, Colo., *J. Geophys. Res.*, *115*, G03007, doi:10.1029/2009JG001077.
Lawrence, D. M., et al. (2011), Parameterization improvements and functional and structural advances in version 4 of the Community Land Model, *J. Adv. Model. Earth Syst.*, *30*, M03001, doi:10.1029/2011MS000045.
Lawrence, D. M., K. W. Oleson, M. G. Flanner, C. G. Fletcher, P. J. Lawrence, S. Levis, S. C. Swenson, and G. B. Bonan (2012), The CCSM4 land simulation, 1850–2005: Assessment of surface climate and new capabilities, *J. Clim.*, *25*, 2240–2260, doi:10.1175/JCLI-D-11-00103.1.
Lazaro, F. J., L. Gutiérrez, V. Barrón, and M. D. Gelado (2008), The speciation of iron in desert dust collected in Gran Canaria (Canary Islands): Combined chemical, magnetic and optical analysis, *Atmos. Environ.*, *42*, 8987–8996.
Linke, C., O. Möhler, A. Veres, A. Mohacsi, Z. Bozoki, G. Szabo, and M. Schnaiter (2006), Optical properties and mineralogical composition of different Saharan mineral dust samples: A laboratory study, *Atmos. Chem. Phys.*, *6*, 3315–3323.
Maring, H., D. L. Savoie, M. A. Izaguirre, L. Custals, and J. S. Reid (2003), Mineral dust aerosol size distribution change during atmospheric transport, *J. Geophys. Res.*, *108*(D19), 8592, doi:10.1029/2002JD002536.
Marshall, S., and R. J. Oglesby (1994), An improved snow hydrology for GCMs. Part 1: Snow cover fraction, albedo, grain size, and age, *Clim. Dyn.*, *10*, 21–37.
Marshall, S. E. (1989), A physical parameterization of snow albedo for use in climate models, NCAR cooperative thesis 123, 175 pp., Natl. Cent. for Atmos. Res., Boulder, Colo.
Marshall, S. E., and S. G. Warren (1987), Parameterization of snow albedo for climate models, in *Large Scale Effects of Seasonal Snow Cover*, IAHS Publ., vol. 166, edited by B. E. Goodison, R. G. Barry, and J. Dozier, pp. 43–50, International Association of Hydrological Sciences, Washington, D. C.
Matzl, M., and M. Schneebeli (2006), Measuring specific surface area of snow by near-infrared photography, *J. Glaciol.*, *52*, 558–564.
Matzl, M., and M. Schneebeli (2010), Stereological measurement of the specific surface area of seasonal snow types: Comparison to other methods, and implications for mm-scale vertical profiling, *Cold Reg. Sci. Technol.*, *64*, 1–8.
McClatchey, R. A., R. W. Fenn, J. F. A. Selby, F. E. Volz, and J. S. Garing (1972), *Optical Properties of the Atmosphere*, *Rep. AFCRL-72-0497*, 108 pp., 3rd ed., Air Force Geophysics Laboratory, Hanscom, Mass.
McConnell, C. L., P. Formenti, E. J. Highwood, and M. A. J. Harrison (2010), Using aircraft measurements to determine the refractive index of Saharan dust during the DODO experiments, *Atmos. Chem. Phys.*, *10*, 3081–3098.
McConnell, J. R., R. Edwards, G. L. Kok, M. G. Flanner, C. S. Zender, E. S. Saltzman, J. R. Banta, D. R. Pasteris, M. M. Carter, and J. D. W. Kahl (2007), 20th century industrial black carbon emissions altered Arctic climate forcing, *Science*, *317*, 1381–1384, doi:10.1126/science.1144856.
Meland, B., P. D. Kleiber, V. H. Grassian, and M. A. Young (2011), Visible light scattering study at 470, 550, and 660 nm of components of mineral dust aerosol: Hematite and goethite, *J. Quant. Spectros. Radiat. Transfer*, *112*, 1108–1118, doi:10.1016/j.jqsrt.2010.12.002.
Ming, J., C. Xiao, H. Cachier, D. Qin, X. Qin, Z. Li, and J. Pu (2009), Black carbon (BC) in the snow of glaciers in west China and its potential effects on albedos, *Atmos. Res.*, *92*, 114–123.
Ming, J., C. Xiao, Z. Du, and X. Yang (2013), An overview of black carbon deposition in High Asia glaciers and its impacts on radiation balance, *Adv. Water Res.*, *55*, 80–87.
Mlawer, E. J., and S. A. Clough (1997), On the extension of rapid radiative transfer model to the shortwave region, in *Proceedings of Sixth Atmospheric Radiation Measurement (ARM) Science Team Meeting*, CONF-9603149, pp. 223–226, U.S. Dep. of Energy, Washington, D. C.
Müller, T., A. Schladitz, A. Massling, N. Kaaden, K. Kandler, and A. Wiedensohler (2009), Spectral absorption coefficients and imaginary parts of refractive indices of Saharan dust during SAMUM-1, *Tellus, Ser. B*, *61*, 79–95.
Müller, T., A. Schladitz, K. Kandler, and A. Wiedensohler (2011), Spectral particle absorption coefficients, single scattering albedos and imaginary parts of refractive indices from ground based in-situ measurements at Cape Verde Island during SAMUM-2, *Tellus, Ser. B*, *63*, 573–588.

Myhre, G., A. Grini, J. M. Haywood, F. Stordal, B. Chatenet, D. Tanré, J. K. Sundet, and I. S. A. Isaksen (2003), Modeling the radiative impact of mineral dust during the Saharan Dust Experiment (SHADE) campaign, *J. Geophys. Res., 10*(D18), 8579, doi:10.1029/2002JD002566.

Neshyba, S. P., T. C. Grenfell, and S. G. Warren (2003), Representation of a nonspherical ice particle by a collection of independent spheres for scattering and absorption of radiation: II. Hexagonal columns and plates, *J. Geophys. Res., 108*(D15), 4448, doi:10.1029/2002JD003302.

Niwano, M., T. Aoki, K. Kuchiki, M. Hosaka, and Y. Kodama (2012), Snow Metamorphism and Albedo Process (SMAP) model for climate studies: Model validation using meteorological and snow impurity data measured at Sapporo, Japan, *J. Geophys. Res.*, *117,* F03008, doi:10.1029/2011JF002239.

Osborne, S. R., B. T. Johnson, J. M. Haywood, A. J. Baran, M. A. J. Harrison, and C. L. McConnell (2008), Physical and optical properties of mineral dust during the Dust and Biomass-burning Experiment, *J. Geophys. Res.*, *113,* D00C03, doi:10.1029/2007JD009551.

Otterman, J., and R. S. Fraser (1976), Earth-atmosphere system and surface reflectivities in arid regions from Landsat MSS data, *Remote Sens. Environ.*, *5*, 247–266.

Painter, T. H., A. P. Barrett, C. C. Landry, J. C. Neff, M. P. Cassidy, C. R. Lawrence, K. E. McBride, and G. L. Farmer (2007), Impact of disturbed desert soils on duration of mountain snow cover, *Geophys. Res. Lett.*, *34*, L12502, doi:10.1029/2007GL030284.

Patterson, E. M., D. A. Gillette, and B. H. Stockton (1977), Complex index of refraction between 300 and 700 nm for Saharan aerosols, *J. Geophys. Res.*, *82*, 3153–3160, doi:10.1029/JC082i021p03153.

Petzold, A., et al. (2009), Saharan dust absorption and refractive index from aircraft-based observations during SAMUM 2006, *Tellus, Ser. B*, *61*, 118–130.

Reid, J. S., et al. (2003), Comparison of size and morphological measurements of coarse mode dust particles from Africa, *J. Geophys. Res., 108*(D19), 8593, doi:10.1029/2002JD002485.

Reist, P. C. (1993), *Aerosol Science and Technology*, McGraw-Hill, New York.

Ricchiazzi, P., S. Yang, C. Gautier, and D. Sowle (1998), SBDART: A research and teaching software tool for plane-parallel radiative transfer in the Earth's atmosphere, *Bull. Am. Meteorol. Soc.*, *79*(10), 2101–2114, doi:10.1175/1520-0477(1998)079<2101:SARATS>2.0.CO;2.

Schwartz, J. P., R. S. Gao, A. E. Perring, J. R. Spackman, and D. W. Fahey (2013), Black carbon aerosol size in snow, *Sci. Rep.*, *3,* 1356, doi:10.1038/srep01356.

Sherman, D. M., and T. D. Waite (1985), Electronic spectra of Fe^{3+} oxides and oxide hydroxides in the near IR to near UV, *Am. Mineral.*, *70*, 1262–1269.

Smith, E. A. (1986), The structure of the Arabian heat low. Part I: Surface energy budget, *Mon. Weather Rev.*, *114*, 1067–1083.

Sokolik, I., A. Andronova, and T. C. Johnson (1993), Complex refractive index of atmospheric dust aerosols, *Atmos. Environ.*, *27A*, 2495–2502.

Sokolik, I. N., and O. B. Toon (1999), Incorporation of mineralogical composition into models of the radiative properties of mineral aerosol from UV to IR wavelengths, *J. Geophys. Res.*, *104*, 9423–9444, doi:10.1029/1998JD200048.

Solmon, F., M. Mallet, N. Elguindi, F. Giorgi, A. Zakey, and A. Konaré (2008), Dust aerosol impact on regional precipitation over western Africa, mechanisms and sensitivity to absorption properties, *Geophys. Res. Lett.*, *35*, L24705, doi:10.1029/2008GL035900.

Stamnes, K., S.-C. Tsay, W. Wiscombe, and K. Jayaweera (1988), Numerically stable algorithm for discrete-ordinate-method radiative transfer in multiple scattering and emitting layered media, *Appl. Opt.*, *27*(12), 2502–2509.

Tsay, S. C., and K. Jayaweera (1984), Physical characteristics of Arctic stratus clouds, *J. Clim. Appl. Meteorol.*, *23*(4), 584–596.

Wagner, R., T. Ajtai, K. Kandler, K. Lieke, C. Linke, T. Müller, M. Schnaiter, and M. Vragel (2012), Complex refractive indices of Saharan dust samples at visible and near UV wavelengths: A laboratory study, *Atmos. Chem. Phys.*, *12*, 2491–2512.

Wang, X., S. J. Doherty, and J. Huang (2013), Black carbon and other light-absorbing impurities in snow across northern China, *J. Geophys. Res. Atmos.*, *118*, 1471–1492, doi:10.1029/2012JD018291.

Warren, S. G. (1984), Optical constants of ice from the ultraviolet to the microwave, *Appl. Opt.*, *23*, 1206–1225.

Warren, S. G. (2013), Can black carbon in snow be detected by remote sensing?, *J. Geophys. Res. Atmos.*, *118*, 779–786, doi:10.1029/2012JD018476.

Warren, S. G., and R. E. Brandt (2008), Optical constants of ice from the ultraviolet to the microwave: A revised compilation, *J. Geophys. Res.*, *113*, D14220, doi:10.1029/2007JD009744.

Warren, S. G., and A. D. Clarke (1990), Soot in the atmosphere and snow surface of Antarctica, *J. Geophys. Res.*, *95*, 1811–1816, doi:10.1029/JD095iD02p01811.

Warren, S. G., and W. J. Wiscombe (1980), A model for the spectral albedo of snow. II: Snow containing atmospheric aerosols, *J. Atmos. Sci.*, *37*, 2734–2745.

Warren, S. G., and W. J. Wiscombe (1985), Dirty snow after nuclear war, *Nature*, *313*, 467–470.

Wiscombe, W. J. (1980), Improved Mie scattering algorithms, *Appl. Opt.*, *19*, 1505–1509.

Wiscombe, W. J., and S. G. Warren (1980), A model for the spectral albedo of snow. I: Pure snow, *J. Atmos. Sci.*, *37*, 2712–2733.

Yasunari, T. J., R. D. Koster, K.-M. Lau, T. Aoki, Y. C. Sud, T. Yamazaki, H. Motoyoshi, and Y. Kodama (2011), Influence of dust and black carbon on the snow albedo in the NASA Goddard Earth Observing System version 5 land surface model, *J. Geophys. Res.*, *116*, D02210, doi:10.1029/2010JD014861.

Yasunari, T. J., K.-M. Lau, S. P. P. Mahanama, P. R. Colarco, A. M. da Silva, T. Aoki, K. Aoki, N. Murao, S. Yamagata, and Y. Kodama (2014), Goddard Snow Impurity Module (GOSWIM) for the NASA GEOS-5 Earth System Model: Preliminary comparisons with observations in Sapporo, Japan, *SOLA*, *10*, 50–56, doi:10.2151/sola.2014-011.

Ye, H., R. Zhang, J. Shi, J. Huang, S. G. Warren, and Q. Fu (2012), Black carbon in seasonal snow across northern Xinjiang in northwestern China, *Environ. Res. Lett.*, *7*, 044002, doi:10.1088/1748-9326/7/4/044002.

Zender, C. S., H. Bian, and D. Newman (2003), Mineral Dust Entrainment and Deposition (DEAD) model: Description and 1990s dust climatology, *J. Geophys. Res., 108*(D14), 4416, doi:10.1029/2002JD002775.

Zhang, R., D. A. Hegg, J. Huang, and Q. Fu (2013), Source attribution of insoluble light-absorbing particles in seasonal snow across northern China, *Atmos. Chem. Phys.*, *13*, 6091–6099, doi:10.5194/acp-13-6091-2013.

Zhao, C., X. Liu, R. Leung, and S. Hagos (2011), Radiative impact of mineral dust on monsoon precipitation variability over West Africa, *Atmos. Chem. Phys.*, *11*, 1879–1893.